

## REPORT DOCUMENTATION PAGE

Form Approved  
OMB No. 0704-0188

Public reporting burden for this collection of information is estimated to average 1 hour per response, including the time for reviewing instructions, searching existing data sources, gathering and maintaining the data needed, and completing and reviewing the collection of information. Send comments regarding this burden estimate or any other aspect of this collection of information, including suggestions for reducing this burden, to Washington Headquarters Services, Directorate for Information Operations and Reports, 1215 Jefferson Davis Highway, Suite 1204, Arlington, VA 22202-4302, and to the Office of Management and Budget, Paperwork Reduction Project (0704-0188), Washington, DC 20503.

1. AGENCY USE ONLY (Leave blank)	2. REPORT DATE	3. REPORT TYPE AND DATES COVERED
	July 23, 1997	Final Technical Report 3-1-95 to 2-28-97
4. TITLE AND SUBTITLE		5. FUNDING NUMBERS
Large Capacity PIV Diagnostic Facility for Turbulence Research		F49620-95-1-0197
6. AUTHOR(S)		
RONALD J. ADRIAN		
7. PERFORMING ORGANIZATION NAME(S) AND ADDRESS(ES)		AFOSR-TR-97 C338
University of Illinois Department of Theoretical And Applied Mechanics 216 Talbot Laboratory 104 South Wright Street Urbana, IL 61801		
9. SPONSORING/MONITORING AGENCY NAME(S) AND ADDRESS(ES)		10. SPONSORING/MONITORING AGENCY REPORT NUMBER
AFOSR/NA 110 DUNCAN AVENUE SUITE B115 BOLLING AFB DC 20332-8050		F49620-95-1-0197

11. SUPPLEMENTARY NOTES	12a. DISTRIBUTION AVAILABILITY STATEMENT	12b. DISTRIBUTION CODE
	Approved for public release; distribution unlimited.	19971002 015

13. ABSTRACT (Maximum 200 words)	<p>The purpose of this grant was to construct a stereographic particle image velocimeter (SPIV) for the measurement of three-dimensional velocity vectors on planar slices through fluids defined by laser light sheets. The facility has been constructed from components, requiring the use of multiple vendors. A stereographic particle image velocimeter using two 2,048 x 2,048 pixel video cameras has been constructed and shown to work. An attached paper by Liu, Adrian, and Meinhart (1996) described the system and demonstrated its applicability to turbulence research. The system was used in 1996 to make measurements in planes parallel to the wall of a turbulent boundary layer, at the UIUC boundary layer wind tunnel in order to study the low speed streak spacing of boundary layers and their contribution to the Reynolds shear stress. It was also installed in the National Diagnostic Facility of the Illinois Institute of Technology for use in a collaborative study of non-equilibrium turbulent boundary layers. The system is one-of-a-kind, and it has been an unqualified success.</p>	
----------------------------------	--	--

14. SUBJECT TERMS	DTIC QUALITY INSPECTED 4		15. NUMBER OF PAGES
17. SECURITY CLASSIFICATION OF REPORT	18. SECURITY CLASSIFICATION OF THIS PAGE	19. SECURITY CLASSIFICATION OF ABSTRACT	20. LIMITATION OF ABSTRACT
Unclassified	Unclassified	Unclassified	UL

**FINAL TECHNICAL REPORT**  
**AIR FORCE OFFICE OF SCIENTIFIC RESEARCH**  
**GRANT F49620-95-1-0197**

**Large Capacity PIV Diagnostic Facility for Turbulence Research**

RONALD J. ADRIAN  
University of Illinois  
Department of Theoretical and Applied Mechanics  
216 Talbot Laboratory  
104 South Wright Street  
Urbana, Illinois 61801

July 23, 1997

## Summary

The purpose of this grant was to construct a stereographic particle image velocimeter (SPIV) for the measurement of three-dimensional velocity vectors on planar slices through fluids defined by laser light sheets. The facility has been constructed from components, requiring the use of multiple vendors. A stereographic particle image velocimeter using two 2,048 x 2,048 pixel video cameras has been constructed and shown to work. The attached paper by Liu, Adrian, and Meinhart (1996) describes the system and demonstrates its applicability to turbulence research. The system was used in 1996 to make measurements in planes parallel to the wall of a turbulent boundary layer, at the UIUC boundary layer wind tunnel in order to study the low speed streak spacing of boundary layers and their contribution to the Reynolds shear stress. It was also installed in the National Diagnostic Facility of the Illinois Institute of Technology for use in a collaborative study of non-equilibrium turbulent boundary layers. The system is one-of-a-kind, and it has been an unqualified success.

A cost extension of the grant until January 31, 1997 was requested and approved to permit completion of the entire system. The computer system used for the first, current version of the system was not fast enough to make feasible the analysis of large data bases of vector data, and the technical capabilities of the 2k x 2k cameras did not allow for the determination of the direction of the velocity vectors. The extension was needed to give time to specify and acquire a new, significantly faster computer system and new cameras. The new system has cross-correlating cameras that permit the determination of the direction of the flow without using pulse coding.

Lastly, a new method of correcting for distortions which seriously impact the accuracy of the stereo camera was developed. The method is described in the attached manuscript by Soloff, Adrian and Liu (1997), which will appear in Measurement Science and Technology. This method and the camera constructed to implement are now functional, all programming and optical assembly having been completed. It is currently undergoing shakedown and application in a study of mixing by rotating turbine impellers.

Expenditures are consistent with the originally proposed list of equipment, see Table 1. To achieve the speeds needed for large capacity data analysis it was necessary to re-direct some of the funds to be spent in the final year of the grant to the acquisition of the new high speed computer, instead of the Mac and two printers listed toward the bottom of Table 1. Permission to put the remaining funding into the new computer was requested last year. All items purchased under the equipment grant are summarized in Table 1.

The University of Illinois has contributed in excess of \$41,670.80 in matching funds, and TSI, Inc. contributed \$25,000 in software (see attached Report of Gift Received). Additional moneys in excess of \$33,329.20 were derived from non-Federal grants and contracts. The total contribution from these non-AFOSR sources exceeded the \$100,000 level indicated in the original proposal.

## VISUALIZATION OF STRUCTURE IN A TURBULENT BOUNDARY LAYER USING A STEREOSCOPIC PARTICLE IMAGE VELOCIMETER

Z. C. Liu, R. J. Adrian and C. D. Meinhart  
Department of Theoretical and Applied Mechanics  
University of Illinois, Urbana, Illinois 61801

W. Lai  
TSI, Inc., St. Paul, Minnesota 55164

### ABSTRACT

Development of a stereoscopic particle image velocimeter for the measurement of three-dimensional vectors on a planar domain is described. The camera is based on two high-resolution video cameras. Experiments in a turbulent boundary layer at  $Re\theta = 2525$  demonstrate its applicability to the measurement of three-dimensional turbulent flow. In addition to the quantitative value of the out-of-plane component, it is found that having the complete three-dimensional vector also significantly improves the qualitative visualization of the flow.

### 1. INTRODUCTION

The extension of particle image velocimetry to measurement of three-dimensional velocity vector fields is both desirable and achievable. Hinsch (1995) reviews many of the techniques used for three-dimensional measurements. In general, there are two classes of measurement techniques: those which measure three-dimensional velocity vectors on full three-dimensional domains, i.e. volumes, and those that measure three-dimensional vectors on planar domains, i.e. light sheets. Three-dimensional volumetric measurements can be performed by using holographic techniques (Barnhart *et al.*, 1994, Meng and Hussain, 1995), by using photogrammetric particle tracking techniques (Maas *et al* 1993, Brodkey 1977, Nishino *et al* 1991), or by scanning laser light sheets rapidly (Brucker 1995). Photogrammetric methods use three or four cameras to view particles from several different directions. Volumetric measurements are in general difficult and require equipment that is rather different than the standard planar PIV equipment using a laser light sheet and a single camera. Holographic systems require a unique set of techniques and apparatus, and three-dimensional particle tracking systems involve multiple cameras and specialized software, plus they place demands on the optical access required to view the flow field. However, the most demanding aspect of volumetric measurements is the sheer number of velocity vectors that are obtained from the measurements. A modest  $100 \times 100 \times 100$  velocity grid measurement yields one million vectors, and if these measurements are to be repeated hundreds or even thousands of times for the purpose of statistical averaging, the amount of data is overwhelming. Thus, while volumetric measurements can be extraordinarily valuable for studying instantaneous flow field structures,

they are often too rich in data to be used on a routine basis with present equipment.

An intermediate approach to three-dimensional measurements with PIV is to perform measurements of a three-dimensional velocity field on a planar domain. In this way, the number of vectors is the same as in ordinary two-dimensional planar PIV, but the third component contributes significantly to the experimenter's capability to visualize the flow, and the third component is valuable for the purposes of quantitative analysis of the flow. Further, full measurement of the three-dimensional vectors eliminates the perspective error that is inherent in monocular PIV systems (Adrian 1991, Prasad and Adrian 1993). This error can be quite significant if the flow has significant out-of-plane velocity component and the angular field-of-view is not small.

Systems operating with this capability can be designed using various aspects of image correlation (Robinson and Rockwell 1993), or the change in image magnification (Willert and Gharib 1992). However, the most common technique is the well-known stereoscopic method whereby one obtains a pair of images, each image viewing the particles in the illuminated light sheet plane from a different direction. Displacements of the particle images in the two different views differ because of the different viewing angles, and measurements of these displacements can be used to solve for the full three-dimensional displacement of particles. This technique can be applied to individual particles, as in particle tracking systems, or it can be applied to correlation technique for groups of particles. The correlation approach is desirable because three-dimensional velocity vectors can also be obtained on uniform grids, and the problem of matching individual pairs is solved automatically accounted. The limitation of this technique is that to assure good measurements of the out-of-plane component of velocity, the viewing angles between the stereo lenses must be substantial, of the order of thirty degrees, and the time between exposures of the images must be small enough that the particles remain within the thickness of the light sheet. These requirements have been explored amply and shown to be achievable and not inconvenient in practice (Troy 1994).

Stereographic systems of conventional form have been used by Arroyo and Greated (1991), Prasad and Adrian (1993), and Troy (1994). These experiments each used two photographic recordings, interrogated the

recordings to obtain displacements and then solved the stereo equations to obtain three-dimensional velocity vectors. The difficulty with using photographic film is the problem of registering the two pieces of film with respect to each other so that measurements of displacements locations in the first image can be identified precisely with locations in the second. This problem must be faced for each pair of photographic exposures that are taken in a stereo-photographic system. The registration process is more laborious and time consuming than developing the film itself, and it places a fundamental constraint on the utility of this method.

To make feasible extensive quantitative analysis of three-dimensional vector fields, it is necessary to make the image acquisition analysis process easy enough and fast enough to permit thousands of images to be taken for averaging purposes. To this end, the photographic recording must be eliminated, and replaced by videographic recording. Video cameras in a stereo system can be registered during the construction of the stereo camera and by this means they can be aligned once and for all, thereby eliminating all future efforts at registering the two images. The registration can be accomplished both by means of mechanical alignment during construction, and by electronic image processing alignment during the experimental stage. The electronic alignment is necessary in situations where an aberrating medium is placed between the object plane and the cameras, because the registration that was originally achieved in the construction of the camera is distorted by the medium. In this case, a calibration procedure can be used to correct for aberrations, provided they are not so severe as to completely destroy the images of the individual particles.

In this paper, the design and construction of a stereographic camera based on video recording is described, and some of the procedures used in the aberration calibration and correction process are explained. The system is applied to the visualization of three-dimensional vector field structure in a low Reynolds number turbulent boundary layer.

## 2. STEREOSCOPIC PIV SYSTEM

The stereoscopic camera is shown schematically in Fig. 1. The camera lenses  $L_1$  and  $L_2$  lie in a plane parallel to the object plane defined by the laser light sheet. They are offset laterally by  $d_{L1}$  and  $d_{L2}$ , respectively. Since the camera arrays also lie in a plane parallel to the object plane, the magnification of each lens is constant, equal to

$$M_0 = d_i / d_o, \quad (1)$$

where  $d_i$  and  $d_o$  are the image and object distances, respectively. Within the angular field indicated by the solid lines each lens images point objects with resolution and distortion that are within the specification of the lens. In the object plane the size of the region that can be imaged with good resolution by both lenses, the 'joint field', is determined by the intersection of the respective angular fields. The lateral offsets  $d_{L1}$  and  $d_{L2}$  are chosen to be the largest values

that still permit the angular fields to overlap over the desired region in the object plane, i.e. to make the joint field as large as possible while still keeping the angle between the lenses large enough to achieve small measurement error for the z-component of velocity. Nominally,  $d_{L1}$  and  $d_{L2}$  are equal, and the angle between the axes of the two lenses is 24.4 degrees. According to Prasad and Adrian (1993) the error in the z-component of velocity is about twice the error in the in-plane components of velocity when the angle between the axes of the lenses exceeds 30 degrees.

The field of view of each CCD array is simply the area of the array mapped onto the object plane. As in Prasad and Adrian (1993) and Troy (1994), offsetting the cameras laterally in the image plane overlaps their respective fields of view. Each camera sees nearly the same region in the flow, thereby maximizing the size of the joint field of view. This design is relatively simple to layout, but care must be taken to ensure that tolerances in the focal lengths of the lenses and in the orientations of the individual elements of the system are taken into account, either mechanically, or by careful calibration.

The joint field of view increases by more than a factor of two if the lenses are tilted towards each other so as to completely overlay their angular fields. This method, called 'angular displacement', has been discussed by Gauthier and Riethmuller (1988) and more recently by Prasad and Jensen (1996). Its principle advantage is the larger joint field of view, and its principal disadvantage is the more complicated alignment that is needed, which also involves using magnification that varies across the field of view. Only the simpler lateral offset method will be considered here, although angular offset can be easily accommodated by the present camera.

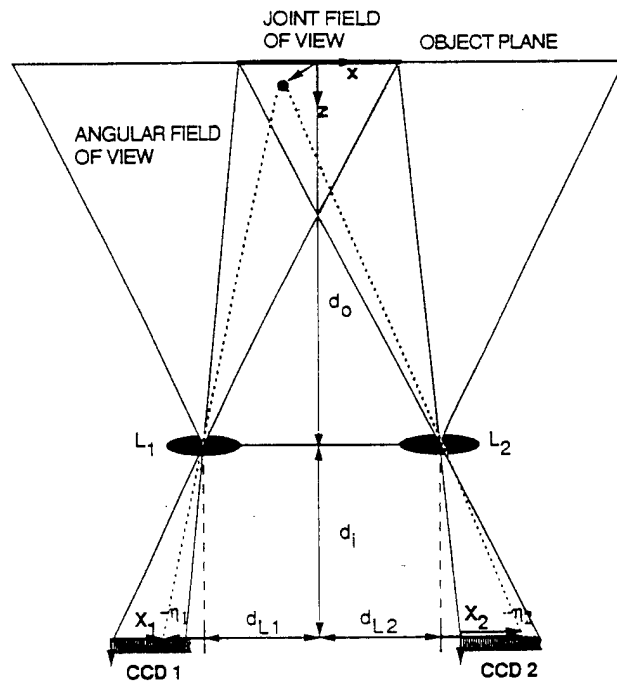


Figure 1. Schematic of the stereoscopic camera.

The camera uses two Kodak *Megaplus* 4.2 CCD video cameras, each with 2029 x 2044 pixels resolution. Since the camera is intended to image a 100-300 mm field of view in the flow, and the CCD chip dimension is only 18 mm, the magnification of the system is substantially less than unity.  $M = 0.23$  for the present system. Two Nikon *EL-Nikkor* 302.5 mm F/5.6 enlarging lenses that are optimized for normal operation at large magnification are utilized to provide the appropriate small magnification with little aberration, minimal distortion and large aperture (53.6 mm). The angular field of view of this lens is 57 degrees. Images are normally acquired at F/9. The video cameras and two lenses are mounted on a 3-D translation stage. The stage provides the six degrees of freedom needed to position and focus the cameras and to accurately register them with respect to each other. For the wind tunnel experiments,  $D_o = 1617$  mm and  $d_i = 372$  mm.

The rest of the stereoscopic system is shown in Fig. 2. Illumination of the flow field is provided by two Continuum Lasers Nd:YAG lasers with a wavelength of 532 nm at pulse frequency of 10 Hz. Each laser delivers up to 200 mJ/pulse of energy with a pulse duration of 8 nsec. The laser beam is formed into a sheet of about 1 mm thickness in the test section. To resolve directional ambiguity, image shifting is normally needed. However image shifting was not used for the present measurements because of the strong mean flow in comparison with the turbulence intensity in the boundary layer. If directional ambiguity were a problem the cameras could be replaced by 1k x 1k cross-correlating camera. Timing for the sequence of laser pulses and the image capture with the cameras is provided by a TSI, Inc. *Laser Pulse* synchronizer box.

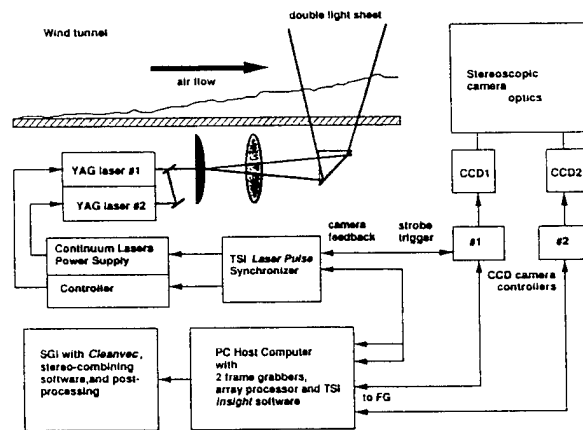


Figure 2. Stereoscopic system.

### 3. IMAGE ANALYSIS

The image analysis procedure is described in Fig. 3. The capture and analysis of images is controlled by *INSIGHT*, a Windows-based software package supplied by TSI, Inc. The software controls the simultaneous image capture by the video cameras. Image analysis to determine the velocity vectors on each image plane is performed by the autocorrelation technique. The outcome of the analysis is a pair of displacement vector fields,

$\Delta X_1$  and  $\Delta X_2$  that are functions of the camera coordinates,  $X_1$  and  $X_2$ . The vectors in these fields are tested for validity using procedures described by Meinhart, *et al.* (1996), and invalid vectors are either

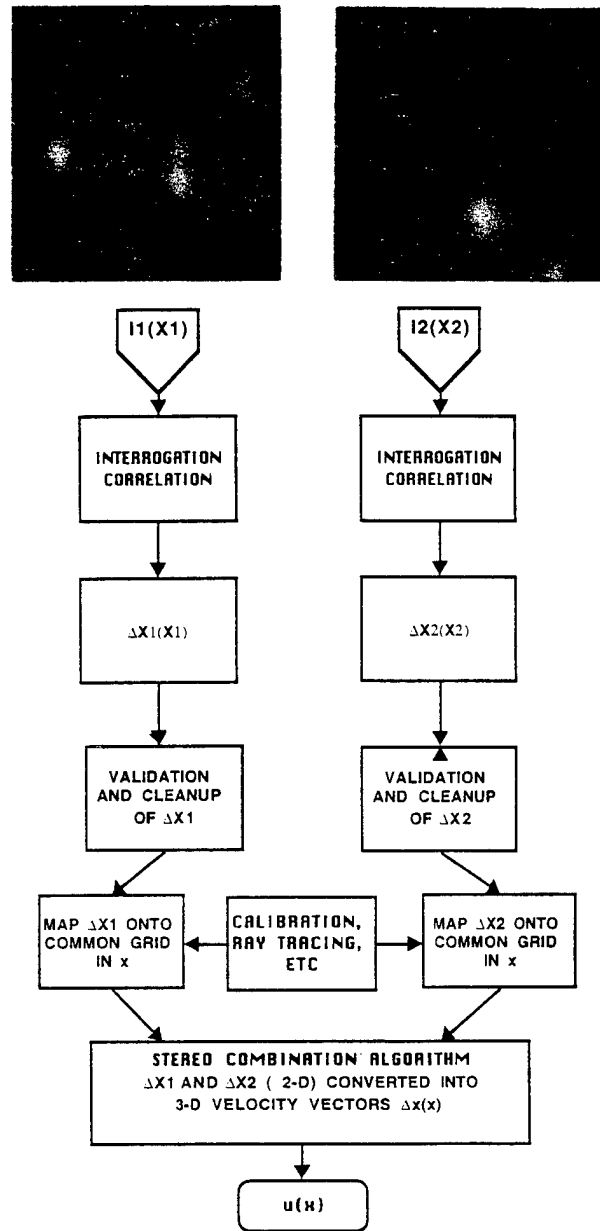
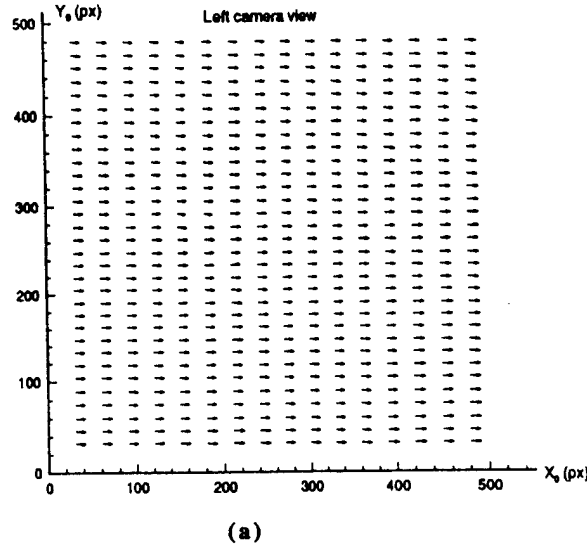


Figure 3. Image analysis procedure.

replaced by second or third choice vectors from the autocorrelation interrogation, replaced by interpolated values, or simply removed. Typically the fraction of invalid vectors is less than 2%. Corrections for the misregistration of the images, and the variation of the magnification factors are all performed in a post-processing package. Effectively, this step maps the displacement vectors from a grid in each of the CCD

array image planes onto a common grid in the object plane. This step is necessary in general if there is any distorting medium between the object plane and the camera, such as a water-air interface (Prasad and Adrian 1993). In the present experiment the 6.35 mm thick glass windows of the wind tunnel cause the images to be displaced laterally by 0.55 mm. Since this shift is nearly constant, it is most easily accounted for by mechanical alignment in the initial layout of the cameras. In more general cases of nonlinear distortion it is better to calibrate the distortion and correct for it in software. The procedures for doing this will be discussed elsewhere.



(a)

Lastly, the stereoscopic equations are applied to compute the third-component of the velocity vectors. For the ideal camera system shown in Fig. 1 the image of a point particle at  $x$  is mapped by lens  $\ell$  onto a location  $\eta_\ell$  in the  $X_\ell$ -plane on camera  $\ell$  given by

$$-\eta_1 = \frac{-d_i}{d_o - z} [(x + d_{L1})\hat{x} + y\hat{y}], \quad (2a)$$

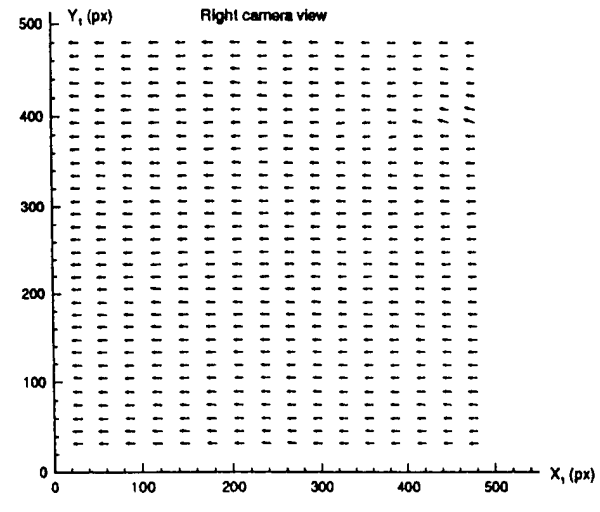
$$-\eta_2 = \frac{-d_i}{d_o - z} [(x - d_{L2})\hat{x} + y\hat{y}] \quad (2b)$$

where carats denote unit vectors. Three-dimensional displacement of the particle by an amount  $\Delta\mathbf{x}$  results in two-dimensional displacements  $\Delta\eta_\ell$  that are found by taking the increment of (2). The result depends on the  $z$ -location of the particle at the time of the first exposure. However, PIV correlation analysis gives an estimate of the *volume average* of the displacements of the particles that lie in the measurement volume defined by the thickness of the light sheet and the area of the interrogation spot. By integrating the equation for the image displacement over such a volume and by making use of the normally large ratio of the object distance to the light sheet thickness, Prasad and Adrian (1993) have

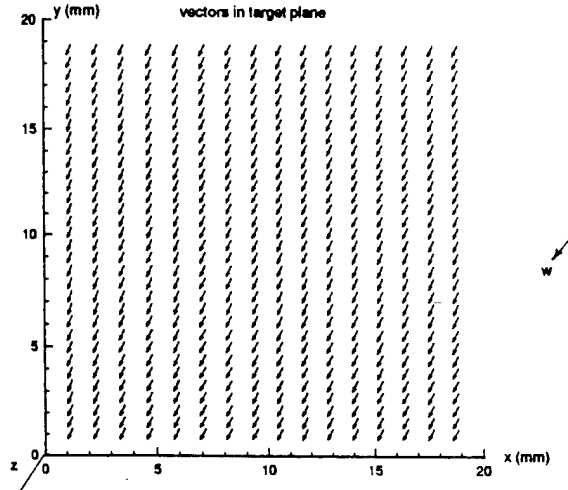
shown that the volume averaged displacements are given by

$$\Delta\bar{\eta}_1 = M_o \left[ \Delta x + \frac{(x + d_{L1})}{d_o} \Delta z \right] \hat{x} + M_o \left[ \Delta y + \frac{y}{d_o} \Delta z \right] \hat{y} \quad (3a)$$

$$\Delta\bar{\eta}_2 = M_o \left[ \Delta x + \frac{(x - d_{L2})}{d_o} \Delta z \right] \hat{x} + M_o \left[ \Delta y + \frac{y}{d_o} \Delta z \right] \hat{y} \quad (3b)$$



(b)



(c)

Figure 4. Image displacement fields due to a pure out-of-plane translation. (a) Camera 1,  $-\eta_1(\mathbf{X}_i)$ ; (b) Camera 2,  $-\eta_2(\mathbf{X}_i)$ ; (c) Three-dimensional displacement field,  $\Delta\mathbf{x}(\mathbf{X})$ .

Given the two two-dimensional vector displacements  $\Delta\eta_1, \Delta\eta_2$  three of the equations in (3) can be solved for  $\Delta x, \Delta y, \Delta z$ , and the fourth can be used to obtain a second estimate of  $\Delta y$ . Alternatively, the two  $\Delta y$ -equations can be added together to obtain a slightly more robust equation. The three-dimensional velocity vector is, of course, found by dividing three dimensional displacement by the time between exposures.

Figure 4a and 4b show the displacement fields that result on cameras 1 and 2, respectively when the object field undergoes a pure, uniform displacement in the  $z$ -direction. Solving equation (3) for the three-dimensional particle displacement yields the field shown in Fig. 4c.

#### 4. TURBULENT BOUNDARY LAYER MEASUREMENTS

The turbulent boundary layer measurements were performed in an eiffel-type low-turbulence boundary layer wind tunnel with a working section 914 mm wide  $\times$  457 mm high  $\times$  6.096 m long. The free stream turbulence intensity at the test section inlet is less than 0.2% for free stream velocities less than 10 m/sec. The turbulent boundary layer was produced on a flat plate placed 100 mm above the floor of the test section. The boundary layer was tripped by the a 4.7 mm diameter wire which spanned the boundary layer plate just downstream of the leading edge. Optical access to the boundary layer was provided from the side by float glass windows, and from below by 610 mm wide  $\times$  2.748 m long float-glass windows embedded in the boundary layer plate. The stereo PIV measurements presented here were performed at a free stream velocity of 3.4 m/sec, which produced a Reynolds number based on the momentum thickness  $\theta$  of  $Re\theta=2575$  at the location of the measurements. All measurements were made with the light sheet in the  $x$ - $y$  plane of the flow, where  $x$  is streamwise and  $y$  is normal to the wall.

Figure 5 shows the  $(u, v)$  components of one realization of the flow field. A constant convection velocity of 3000 mm/s has been subtracted to make the fluctuations more visible. The edge of the turbulent boundary layer lies around 50 mm above the wall in this realization. As observed in earlier work, there is an internal layer close to the wall that grows in a manner similar to that of an ordinary boundary layer. This internal layer, seen as a region of uniformly low momentum that extends from the wall up to about 20 mm, is capped by a collection of several intense spanwise vortices.

The  $w$ -component of velocity is shown in Figure 6 by plotting its contours in gray-level form. It is immediately clear that the values of the  $w$ -component are frequently as large or larger than the other components. There is a tendency for the  $w$ -contours to align along the same 30 degree inclination that is observed in the  $u$ - $v$  field. There is also a tendency for the sign of the  $w$ -component to be positive on one side of a 30 degree line and negative on the other, indicating a large-scale rotation about an inclined axis. The strength of the  $w$ -component and its coherent organization shows that one

must be very cautious in interpreting the two-dimensional fields in a data set such as Figure 5.

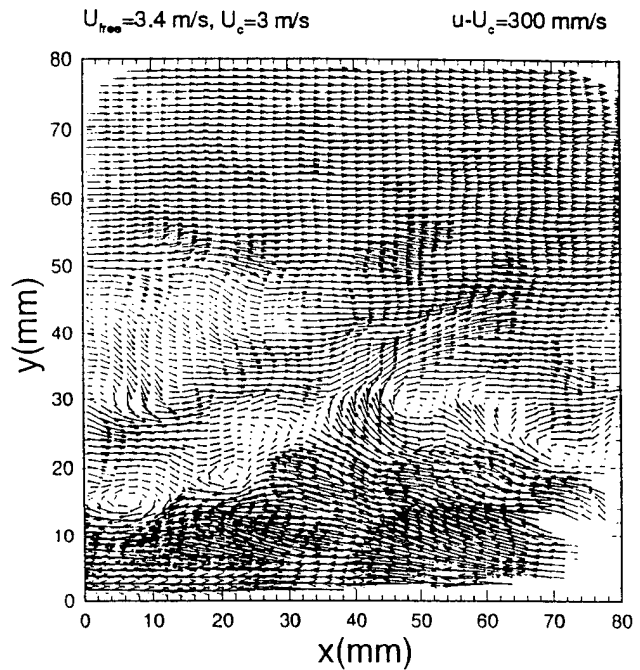


Figure 5. Streamwise-wall normal vector field of the turbulent boundary layer.

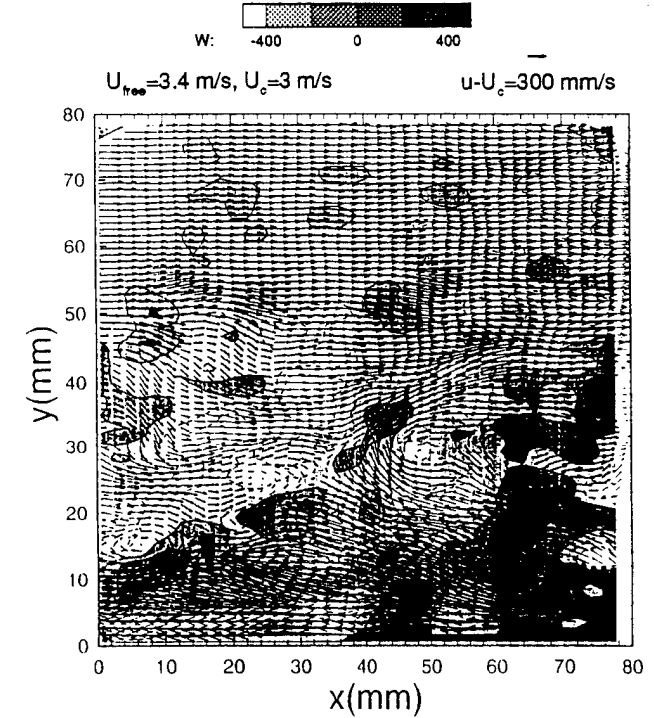


Figure 6. Field of the spanwise turbulent velocity superimposed on the streamwise-wall normal field from Fig. 5.

The three dimensional vectors are shown in end view, i.e. looking at the  $x$ - $y$  plane along the  $x$ -axis, in

Figure 7a, and in oblique view in Figure 7b. The growth of the internal low-momentum layer is very evident in Figure 7b.

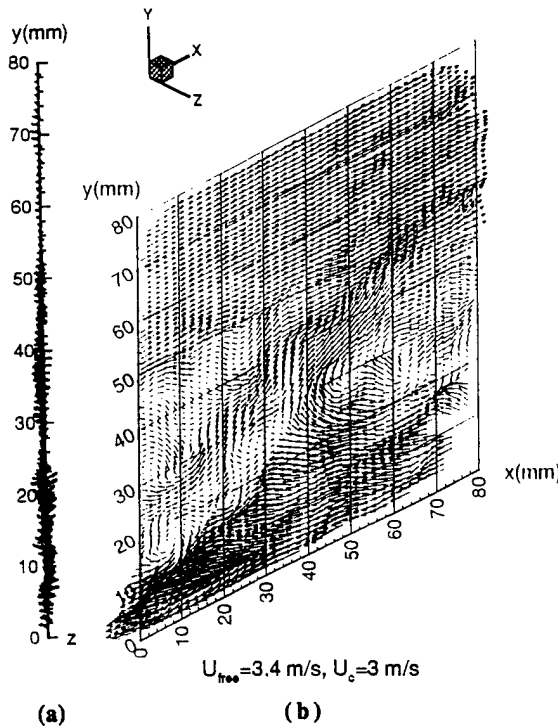


Figure 7. Three-dimensional vectors on the  $x$ - $y$  plane.  
(a) end view; (b) oblique view.

## 5. SUMMARY

Stereoscopic PIV corrects for perspective error as well as providing the out-of-plane component. It requires a special camera, but otherwise it uses essentially the same hardware as a monocular PIV. Videographic recording increases the ease of use substantially by eliminating the necessity of registering photographic images. The present system has been used to measure thousands of frames in experiments that required only a few days to set up. Although the video-based PIV system has less resolution than a photographic system, it is encouraging that it is still able to resolve many of the important features of the turbulent boundary layer that have only recently been discovered by photographic PIV. The results are very similar to those obtained by photographic PIV. Thus, while the video system clearly has a role to play in the acquisition of data for analysis by statistical averaging, it also provides enough resolution to be of considerable value in visualizing the flow.

## Acknowledgments

This work was supported by the United States Air Force Office of Scientific Research, the United States Office of Naval Research, and TSI, Inc.

## References

Adrian, R. J. 1991, Particle-imaging techniques for experimental fluid mechanics, *Ann. Rev. Fluid Mech.*, vol. 23, pp. 261-304.

Arroyo, M.P. and Greater, C.A., 1991, Stereoscopic particle image velocimetry, *Meas. Sci. Tech.* Vol. 2, pp. 1181-1186.

Barnhart, D.H., Adrian, R.J. and Papen, G.C., 1994, Phase-conjugate holographic system for high resolution particle image velocimetry, *Appl. Opt.*, Vol. 33, pp. 7159-7170.

Brodkey, R.S., 1977, Stereoscopic visual studies of complex turbulence shear flows, *Flow Visualization*, (Ed. Asanuma, T.), New York: McGraw-Hill, pp. 117-122.

Brucker, C., 1995, 3D-PIV using stereoscopy and a scanning light-sheet: application to the 3D unsteady sphere wake flow, *Flow Visualization VII*, (Ed. Crowder, J.P.), New York: Begell House, pp. 715-720.

Gauthier, V. and Riethmuller, M.R., 1988, Application of PIV to complex flows: measurements of the third component. *Von Karman Institute Lecture Series on Particle Image Velocimetry*. Rhodes-Saint-Genese: von Karman Institute for Fluid Dynamics.

Hinsch, K.D., 1995, Three-dimensional particle velocimetry, *Meas. Sci. Tech.* Vol. 6, pp. 741-753.

Meinhart, C.D., Barnhart, D.H. and Adrian, R.J., 1996, Interrogation and Validation of 3-D vector fields, *Development in Laser Techniques and Applications to Fluid Mechanics*, Springer: Berlin, pp. 379-391.

Meng, H. and Hussain, F., 1995, In-line recording and off-axis viewing (IROV) technique for holographic particle velocimetry, *Appl. Opt.* Vol. 34, pp. 1827-1840.

Nishino, Y., Kasagi, S. and Hirata, M., 1989, Three-dimensional particle tracking velocimetry based on automated digital image processing. *ASME J.* Vol. 111, pp. 384-391.

Prasad, A.K., and Adrian, R.J., 1993, Stereoscopic particle image velocimetry applied to liquid flows, *Exp. Fluids*, Vol. 15, pp. 49-60.

Prasad, A.K., Jensen, K., 1995, Saheimpflug stereocamera for particle image velocimetry in liquid flows, *Appl. Opt.*, Vol. 34, pp. 7092-7099.

Robinson, O., and Rockwell, D., 1993, Construction of three-dimensional images of flow structure via particle tracking techniques, *Exp. Fluids*, Vol. 14, pp. 257-270.

Troy, V., 1994, A study of Turbulent Penetrative Thermal Convection Using Stereoscopic Particle Image Velocimetry. *M.S. thesis*, University of Illinois, Urbana.

Willert, C.E., and Gharib, M., 1991, digital particle  
image velocimetry, Exp. Fluids, Vol. 10, pp. 181-193.

# **DISTORTION COMPENSATION FOR GENERALIZED STEREOSCOPIC PARTICLE IMAGE VELOCIMETRY**

**Steven M. Soloff, Ronald J. Adrian, and Zi-Chao Liu**

Department of Theoretical and Applied Mechanics  
University of Illinois at Urbana-Champaign  
Urbana, Illinois, USA 61801

## **Abstract**

Optical distortion caused by inaccurate optical alignment, lens nonlinearity, and/or refraction by optical windows, fluid interfaces, and other optical elements of an experiment cause inaccuracy by introducing variable magnification. Since fractional changes in the magnification have a one-to-one effect on the accuracy of measuring the velocity, it is important to compensate for such distortions. A general experimental calibration procedure is described which determines the magnification matrix of a distorted imaging system, and an algorithm is presented to compute accurate velocity field displacements from measurements of distorted PIV images. These procedures form a basis for generalized stereoscopic PIV procedures which permit easy electronic registration of multiple cameras and accurate recombination of stereoscopic displacement fields to obtain the three-dimensional velocity vector field.

## 1. Introduction

The accuracy of velocity measurement by particle image velocimetry (PIV) or particle tracking velocimetry (PTV) depends upon the accuracy with which image displacements can be measured and the accuracy with which image displacements can be related to particle locations and their respective particle displacements. (A third factor, the accuracy with which particle displacements are equal to fluid displacements, is not considered here.) These factors depend in turn on two types of optical aberrations: focusing aberrations which cause the particle images to be enlarged, making it more difficult to measure displacements accurately, and image distortion which creates a nonlinear relationship between the location of a particle and the location of its image. Focusing aberrations include spherical aberration, astigmatism, and coma (Jenkins and White 1957). Image distortion refers to any agency that causes the magnification to vary as a function of position in the field of the image.

There are three agencies that cause the magnification in an experiment to vary. The first is design imperfection in the lens. The second is refraction caused by anything, including windows and fluid interfaces, that lies between the object plane in the illuminating light sheet and the image plane (c.f. Prasad and Adrian 1993, for example). The third is misalignment of the image recording plane with respect to the object plane. The image recording plane is the surface of the film or the video array on which the image is actually recorded, and it need not coincide with the image plane in which all images are in ideal focus. Even if they do coincide, the magnification is not constant unless the image plane is parallel to the object plane, as in lateral-offset stereoscopic cameras, such as those described in Arroyo and Greated (1991) and Grant *et al.* (1995). This last distortion necessarily occurs in angular-offset stereoscopic cameras in which the image plane is rotated with respect to the object plane in order to bring the images into better focus (Prasad and Jensen 1995). It also occurs in single lens cameras and in lateral-offset stereoscopic cameras due to imperfect alignment of the recording plane with the object plane.

The PIV recording and interrogation processes are illustrated in Fig. 1 for the case of zero distortion. The image of any particle is simply located by the chief ray that extends from the particle through the center of the lens to the image plane. Choosing coordinate systems in the object and image planes with origins  $Ox$  and  $OX$  on the optic axis of the lens, the following simple relationship results:

$$(X, Y) = -M(x, y), \quad (1)$$

where  $\mathbf{X} = (X, Y)$  is the image location and  $(x, y)$  is the object location formed from the projection of  $\mathbf{x} = (x, y, z)$  onto the  $xy$ -plane. The magnification is

$$M = \frac{d_i}{d_o - z}, \quad (2)$$

in which  $d_i$  is the image distance and  $d_o$  is the object distance.

The case of nonzero distortion is illustrated in Fig. 2. Here, a curved window acts like a weak lens to refract the chief ray, and the image recording plane is tilted with respect to the object plane. Both of these effects cause some blurring of the point response image on the recording plane, but as noted above, that blurring may be small enough to permit successful

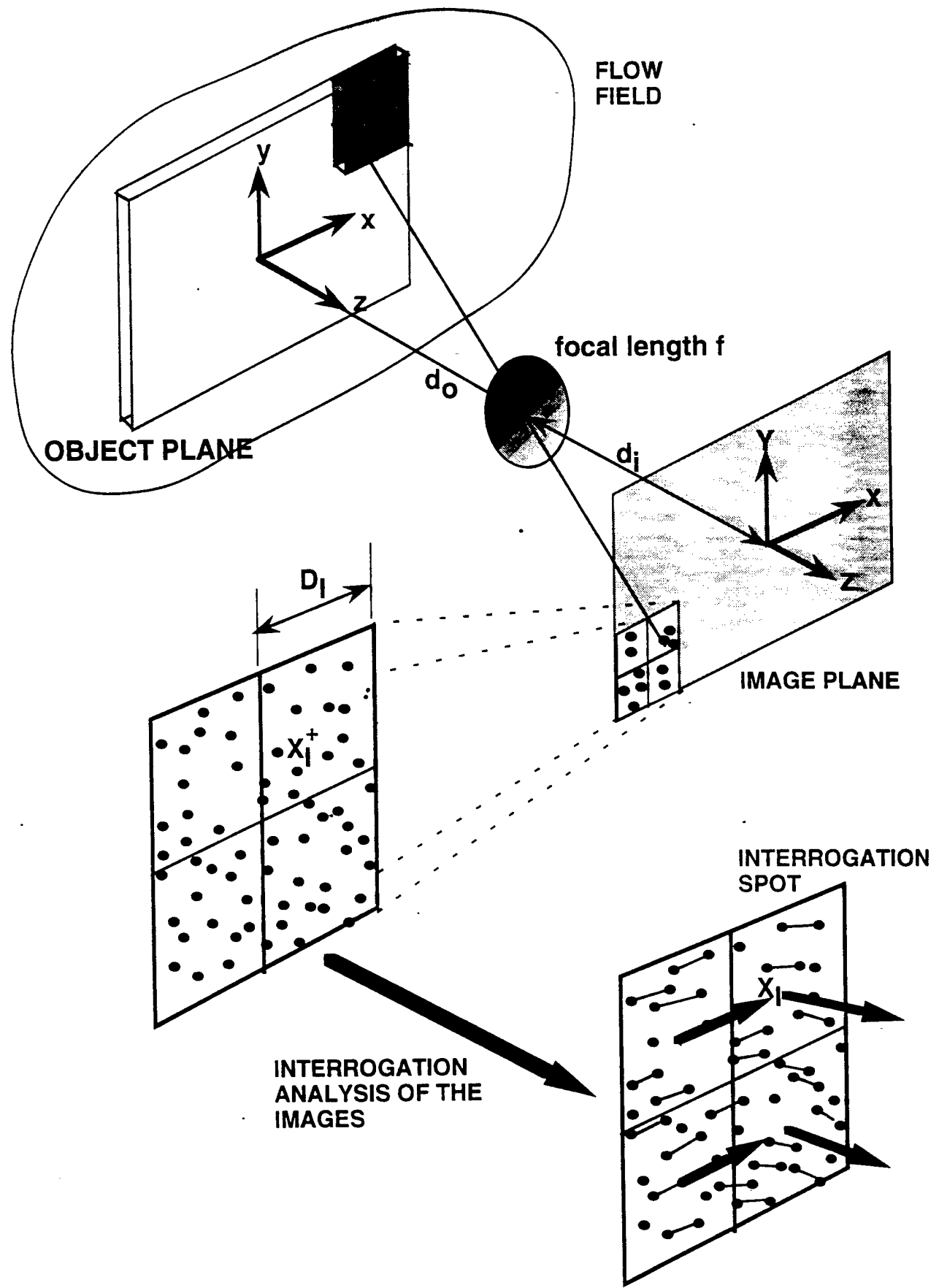


**Figure 1.** PIV recording and interrogation processes for a single camera with zero distortion.  $X_I$  is the location of the center of the interrogation spot on the image plane.

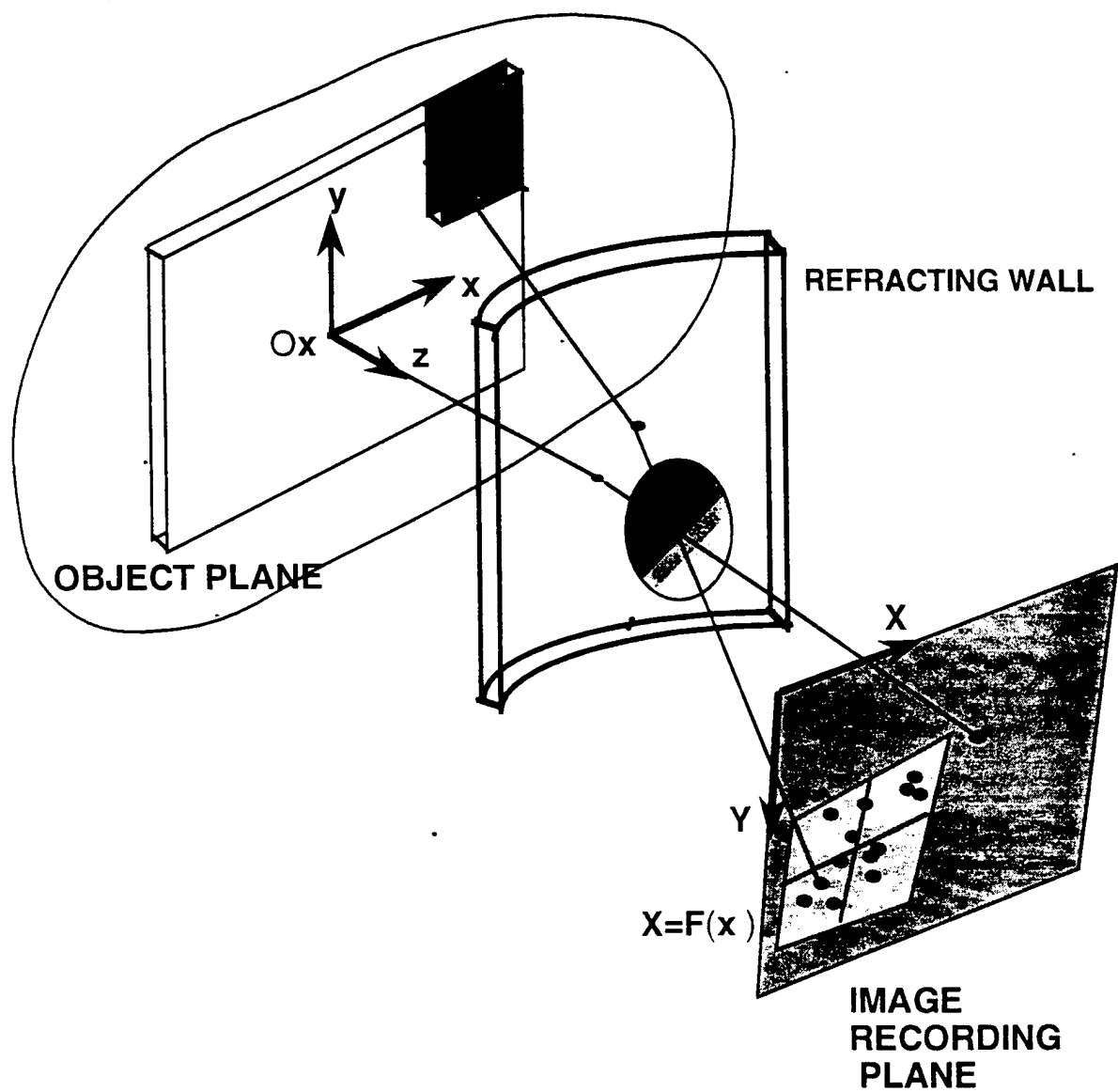


**Figure 2.** PIV recording process for a single camera with nonzero distortion.  $F(x)$  is the mapping function for the camera that relates positions in the object plane to positions in the image plane.

measurement of the image displacements despite significant distortion. The reference frame  $\mathbf{X}$  is embedded in the recording frame, i.e.  $Z = 0$ , and since it is normally associated with the pixel index array, its orientation in this general case with respect to the object plane is allowed to be arbitrary. In general the relationship between positions in the three-dimensional physical space of the flow,  $\mathbf{x}$ , and the positions in the two-dimensional image recording plane,  $\mathbf{X}$ , can be described by a nonlinear mapping function,

$$\mathbf{X} = \mathbf{F}(\mathbf{x}), \quad (3)$$

that replaces the simple linear relationship in Eq. (1). Note that  $\mathbf{x}$  in this equation is the full, three-dimensional vector.

Variable magnification introduces systematic bias errors into the measurement of fluid velocity and the location of the velocity vector. Being systematic, the distortion bias can be corrected by an appropriate technique based either on a mathematical model of the distortion, as in Prasad and Adrian (1993), or on an experimental calibration, as in the calibration for particle tracking velocimetry described by Kent *et al.* (1993). In the work presented here, a calibration is used to generate an approximate mapping function. Distortion can be compensated even when the focusing aberrations cause some blurring of the images, so long as the blurring is not so severe as to make the measurement of image locations impossible or unacceptably inaccurate.

The information found by calibration can be used to do more than correct for distortion. Most PIV interrogation analyses determine the velocity vectors on a uniform grid fixed in the pixel array of the video camera, and the user has no ability to request data on a non-uniform grid *in the fluid* that may be more appropriate for the flow under consideration. A side benefit of using the mapping function algorithm described here is that the measured vectors can be interpolated onto any grid within the domain of the mapping function.

The use of a general mapping function found by calibration is very helpful in the physical construction of a stereoscopic PIV camera because it eliminates the need to mechanically register the pixel arrays of multiple cameras, replacing this process by a simple mathematical registration. In addition, it will be shown how the mathematics of the mapping function provides a natural framework in which to combine the images of two or more cameras to obtain the three-dimensional vector field.

## 2. Displacement Equations

### 2.1 Single Camera

Consider first the displacement of one particle as recorded by a single camera. Following this analysis the results will be generalized to the displacement of groups of particles, as measured by PIV correlation techniques. In the next section, the results will be applied to stereoscopic cameras.

Between exposures at times  $t$  and  $t + \Delta t$  a particle at  $\mathbf{x}$  moves to  $\mathbf{x} + \Delta\mathbf{x}$ . The displacement of its image is

$$\Delta\mathbf{X} = \mathbf{F}(\mathbf{x} + \Delta\mathbf{x}) - \mathbf{F}(\mathbf{x}). \quad (4)$$

To first order the displacement is approximated by

$$\Delta \mathbf{X} \cong \nabla \mathbf{F}(\mathbf{x}) \Delta \mathbf{x}, \quad (5)$$

where the gradient,

$$(\nabla \mathbf{F})_{ij} = \frac{\partial F_i}{\partial x_j} = F_{i,j}, \quad i = 1, 2 \text{ and } j = 1, 2, 3, \quad (6)$$

is clearly a generalization of the usual concept of magnification. We shall call it the *magnification matrix*. As an example, and for later reference, the magnification matrix for perfectly linear imaging is, from Eq. (1),

$$F_{i,j}(\mathbf{x}) = \frac{-d_i}{d_o - z} \begin{pmatrix} 1 & 0 & \frac{x}{d_o - z} \\ 0 & 1 & \frac{y}{d_o - z} \end{pmatrix}. \quad (7)$$

The terms in the last column,  $F_{1,3}$  and  $F_{2,3}$ , represent the effect of perspective.

In PTV the displacement of the image of an individual particle,  $\Delta \mathbf{X}$ , is determined by image analysis, and one must then relate that displacement to displacement in the physical space,  $\Delta \mathbf{x}$ . Eq. (4), or more commonly the approximate Eq. (5), can provide the necessary relationship when distortions are present, but there are two problems in executing the last step. First, since  $\mathbf{X}$  is two-dimensional and  $\mathbf{x}$  is three-dimensional, there is not a unique relationship between  $\mathbf{X}$  and  $\mathbf{x}$ . The particle could lie anywhere along the chief ray that extends from the image point through the center of the lens. Second, since  $F_{i,j}$  is a  $2 \times 3$  matrix, there is no unique inverse solution of (4) or (5) for  $\Delta \mathbf{x}$  in terms of  $\Delta \mathbf{X}$ . These difficulties exist whether the imaging is distorted or not, and they are simply a consequence of the effect of perspective (Adrian 1991). In deep-field PTV (i.e. photogrammetry), the solution is to use two (or possibly more) cameras, each giving measurements of image locations in two directions (Nishino *et al.* 1989, Maas *et al.* 1993, and Guezenne *et al.* 1994). Then, the number of measured image displacements exceeds the number of unknowns and both  $\mathbf{x}$  and  $\Delta \mathbf{x}$  can be found.

In light sheet PIV, the situation is a little different because the thickness of the light sheet,  $\Delta z_o$ , is normally very small compared to the object distance,  $d_o$ , and the width of the field of view in the fluid,  $l$ , may, in certain cases, also be small compared to  $d_o$ . These conditions allow certain approximations to be made. Specifically, consider a PIV measurement of displacement that is made in an interrogation spot centered at  $\mathbf{X}_I$  on the image plane. It is known (Adrian 1988) that a PIV measurement by correlation yields, on average, a measurement of the velocity field of the fluid averaged over a volume consisting of the intersection of the interrogation spot, projected back into the fluid with the thickness of the light sheet,  $\Delta z_o$  (c.f. Fig. 1). This volume is called the *interrogation cell*. The center of the interrogation spot  $\mathbf{X}_I$  maps back into a point that intersects the mid-plane of the light sheet at

$$\mathbf{x}_I = (x_I, y_I, 0), \quad (8)$$

where

$$\mathbf{X}_I = \mathbf{F}(\mathbf{x}_I). \quad (9)$$

This is the center of the interrogation cell, and since  $\mathbf{x}_I$  is two-dimensional ( $z_I = 0$ ) it is possible to associate each  $\mathbf{X}_I$  with a unique  $\mathbf{x}_I$ , thereby resolving the first difficulty cited above.

The first-order relationship between an image plane displacement,  $\Delta\mathbf{X}(\mathbf{X}_I)$ , and object plane displacement,  $\Delta\mathbf{x}(\mathbf{x}_I)$ , is derived by Taylor series expansion of Eq. (4) about the point  $\mathbf{x}_I$ , followed by volume averaging the equation over the interrogation cell, with suitable transformations between  $\mathbf{x}$  and  $\mathbf{X}$ . Denoting averages over the interrogation cells in  $\mathbf{x}$  and  $\mathbf{X}$  by overbars, and neglecting any variation of the magnification matrix over the dimensions of the interrogation cell (justified when the dimensions of the interrogation cell are much smaller than the object distance), one finds the following set of equations:

$$\overline{\Delta\mathbf{X}_i} \cong F_{i,j}(\mathbf{x}_I) \overline{\Delta\mathbf{x}_j}, \quad i = 1, 2 \text{ and } j = 1, 2, 3, \quad (10a)$$

or

$$\begin{pmatrix} \overline{\Delta\mathbf{X}_1} \\ \overline{\Delta\mathbf{X}_2} \end{pmatrix} = \begin{pmatrix} F_{1,1} & F_{1,2} & F_{1,3} \\ F_{2,1} & F_{2,2} & F_{2,3} \end{pmatrix} \begin{pmatrix} \overline{\Delta\mathbf{x}_1} \\ \overline{\Delta\mathbf{x}_2} \\ \overline{\Delta\mathbf{x}_3} \end{pmatrix}. \quad (10b)$$

This is the final operative system of equations for interpreting PIV measurements in the presence of distortion. If the distortion is severely nonlinear, or if very high accuracy is needed in the relationship between  $\overline{\Delta\mathbf{X}}$  and  $\overline{\Delta\mathbf{x}}$ , and justified by the accuracy of the measurements of  $\overline{\Delta\mathbf{X}}$ , this relationship can be improved by retaining higher order terms in the Taylor series expansion. The work presented here assumes that a linear expansion is adequate, as is standard practice in all PIV work done to date.

For the case of a single camera, the system of equations in (10) cannot be solved for  $\Delta\mathbf{x}(\mathbf{x}_I)$  as it stands because there are still only two equations for three unknowns. Common practice in PIV with one camera is to ignore the effect of perspective, as embodied in the terms  $F_{1,3}$  and  $F_{2,3}$ , thereby reducing Eq. (10b) to

$$\begin{pmatrix} \overline{\Delta\mathbf{X}_1} \\ \overline{\Delta\mathbf{X}_2} \end{pmatrix} = \begin{pmatrix} F_{1,1} & F_{1,2} \\ F_{2,1} & F_{2,2} \end{pmatrix} \begin{pmatrix} \overline{\Delta\mathbf{x}_1} \\ \overline{\Delta\mathbf{x}_2} \end{pmatrix}. \quad (11)$$

This is justified if  $F_{1,3}$  and  $F_{2,3}$  are small. Some guidance concerning the magnitude of the perspective effect can be gained by considering the expression for the magnification matrix at  $\mathbf{x}_I$  for perfectly linear imaging:

$$F_{i,j}(\mathbf{x}_I) = \frac{-d_i}{d_o} \begin{pmatrix} 1 & 0 & \frac{x_I}{d_o} \\ 0 & 1 & \frac{y_I}{d_o} \end{pmatrix}. \quad (12)$$

It is clear that the perspective effect is small if  $x_I$  and  $y_I$  are both small compared to  $d_o$  for all values of  $x_I$  and  $y_I$ , i.e. over the full field-of-view. This condition is referred to as *paraxial imaging* (Adrian 1991). It is expected that paraxial imaging will lead to small magnitude of the perspective effect in the case of distorted imaging, as well, but this must be verified in individual cases.

Unfortunately, it is quite common for the paraxial condition to be only weakly satisfied. For example, consider a typical laboratory configuration in which a 100 mm wide field-of-view is imaged at an object distance of 500 mm. The position  $x_1$  varies from -50 mm to +50 mm, implying that  $F_{1,3}$  varies between -0.1 and +0.1. Thus, without correcting for perspective, measurements of the in-plane velocity components are contaminated by as much as 10% of the out-of-plane velocity. If the flow is two-dimensional in the  $xy$ -plane, i.e.  $w = 0$ , there is no error, but if the out-of-plane component is comparable to the in-plane component, errors of order 10% are incurred. Stereoscopic imaging provides the only unconditional solution to the problem of compensating for perspective, and it will be considered in the next section.

## 2.2 Stereoscopic Camera

For a stereoscopic system, two cameras are involved in deriving the displacement equations, which requires a slight change in notation. The displacement of a particle image on camera  $c$ , where  $c = 1, 2$ , is

$$\Delta \mathbf{X}^{(c)} = \mathbf{F}^{(c)}(\mathbf{x} + \Delta \mathbf{x}) - \mathbf{F}^{(c)}(\mathbf{x}). \quad (13)$$

Performing a Taylor series expansion of Eq. (13) and volume averaging over the interrogation cell, similarly to what was done in the previous section, one finds the first-order relationship between an image plane displacement on camera  $c$ ,  $\Delta \mathbf{X}^{(c)}(\mathbf{x}_I)$ , and an object plane displacement,  $\Delta \mathbf{x}(\mathbf{x}_I)$ , to be

$$\overline{\Delta \mathbf{X}_i^{(c)}} \cong F_{i,j}^{(c)}(\mathbf{x}_I) \overline{\Delta x_j}, \quad i = 1, 2 \text{ and } j = 1, 2, 3. \quad (14)$$

Eq. (14) provides a system of equations for each camera. Writing out both sets of equations in full and augmenting them yields

$$\begin{pmatrix} \overline{\Delta \mathbf{X}_1^{(1)}} \\ \overline{\Delta \mathbf{X}_2^{(1)}} \\ \overline{\Delta \mathbf{X}_1^{(2)}} \\ \overline{\Delta \mathbf{X}_2^{(2)}} \end{pmatrix} = \begin{pmatrix} F_{1,1}^{(1)} & F_{1,2}^{(1)} & F_{1,3}^{(1)} \\ F_{2,1}^{(1)} & F_{2,2}^{(1)} & F_{2,3}^{(1)} \\ F_{1,1}^{(2)} & F_{1,2}^{(2)} & F_{1,3}^{(2)} \\ F_{2,1}^{(2)} & F_{2,2}^{(2)} & F_{2,3}^{(2)} \end{pmatrix} \begin{pmatrix} \overline{\Delta x_1} \\ \overline{\Delta x_2} \\ \overline{\Delta x_3} \end{pmatrix}, \quad (15a)$$

or

$$\overline{\Delta \mathbf{X}}_A = (\nabla \mathbf{F})_A \overline{\Delta \mathbf{x}}, \quad (15b)$$

where the subscript  $A$  denotes the appropriate augmented entity. This is the final operative system of equations for a stereoscopic camera for interpreting PIV measurements in the presence of distortion.

Although it appears that the system in (15) is overdetermined, this is not necessarily the case. If no errors are incurred when measuring the image displacements, two of the equations will be dependent simply due to the nature of the optics. For example, if a purely  $x_3$ -displacement is observed by a stereocamera, the perceived  $x_2$ -displacement on both cameras will be identical, but the perceived  $x_1$ -displacement will be in opposite directions on each camera. Thus, the second and fourth equations in (15) will be linearly dependent. Several approaches could then be used to solve the system. For example, the two dependent equations could be added together yielding a solvable system. However, random errors are incurred when

measuring the image displacements, so it may not be the case that two of the equations will be exactly dependent. For the general case where the redundancy is not obvious, a least-squares solution should be used to minimize the squared Euclidean norm of the residual,

$$\varepsilon = \left| \overline{\Delta \mathbf{X}}_A - (\nabla \mathbf{F})_A \overline{\Delta \mathbf{x}} \right|^2. \quad (16)$$

### 3. Procedure for Single Camera

The purpose of the calibration is to determine how positions in the object plane map to positions in the image plane taking into account all aberrations. In order to do this it is necessary to acquire images of a *calibration target* whose location in the object plane is known. Design of the calibration target is the most important part of performing a successful calibration. In general, different experiments may require different calibration targets.

The target must have some sort of characteristic marks on its face. These marks and their corresponding images will define how positions in the object plane map to positions in the image plane. The marks are placed on a precise, evenly spaced Cartesian grid. The size and shape of the target is constrained by the measurement container, but it must be large enough so that the characteristic marks occupy the entire field of view of the camera. In order to maximize the accuracy of the mapping function the field of marks should extend to the edges of the viewable field.

In general, the grid on the calibration target has two parameters: (1) the total number of points, and (2) the spacing between points (the size of a grid cell). These parameters should be chosen according to the size of the image acquisition area and the amount of distortion in the experiment. Thus, the number of grid points is proportional to the size of the image acquisition area, while the size of a grid cell is inversely proportional to the amount of distortion in the experiment.

A sometimes attractive alternative to a calibration grid is a single target point that can be moved precisely to many different locations. For example, Kent *et al.* (1993) describe a target on the end of an arm under control of a stepper motor. This approach is very useful for measuring the mapping function over a deep volume, as in photogrammetric PTV.

Ideally, one would like to find a mapping function  $\mathbf{F}$  such that given any point  $\mathbf{x}$  in the object plane, its corresponding location  $\mathbf{X}$  in the image plane could be determined with complete accuracy. In reality, one cannot experimentally determine an  $\mathbf{F}$  that will yield zero error for an arbitrarily complex geometry. Thus, an estimate for the mapping function,  $\hat{\mathbf{F}}$ , that has an analytic representation will be sought instead. Many possibilities arise at this point, but because of its simplicity, a multi-dimensional polynomial is an obvious choice. There are several ways to determine the polynomial. For example, one could use the method of least-squares to determine an  $\hat{\mathbf{F}}$  that approximates the data while minimizing the mean square error,

$$\varepsilon = \frac{1}{N_c} \sum_{\{\mathbf{x}_c\}} \left| \mathbf{F}(\mathbf{x}_c) - \hat{\mathbf{F}}(\mathbf{x}_c) \right|^2, \quad (17)$$

where the set  $\{\mathbf{x}_c\}$  represents the collection of points on the calibration target, and  $N_c$  is the total number of points in the set. Alternatively, an interpolating spline could be used to determine local polynomials.

In all respects, the least-squares polynomial is the easiest form to implement and yields very good results unless the distortion is extremely severe. In these instances, a spline would be a better choice. A least-squares polynomial with cubic dependence in  $x_1$  and  $x_2$ , but quadratic dependence in  $x_3$ , will be adopted as the mapping function estimate for the remainder of this paper. That is,

$$\hat{F}(x) = a_0 + a_1 x_1 + a_2 x_2 + a_3 x_3 + a_4 x_1^2 + a_5 x_1 x_2 + a_6 x_2^2 + a_7 x_1 x_3 + a_8 x_2 x_3 + a_9 x_3^2 + a_{10} x_1^3 + a_{11} x_1^2 x_2 + a_{12} x_1 x_2^2 + a_{13} x_2^3 + a_{14} x_1^2 x_3 + a_{15} x_1 x_2 x_3 + a_{16} x_2^2 x_3 + a_{17} x_1 x_3^2 + a_{18} x_2 x_3^2, \quad (18)$$

where the  $a_i$  are vector-valued coefficients to be determined. It is noted, however, that the generalization to other methods of interpolation or approximation is trivial and should be done if it is warranted by the severity of the distortion.

Choosing  $\hat{F}$  to be a cubic function of  $x_1$  and  $x_2$  was a decision based purely on qualitative information. By viewing a Cartesian grid through various types of distorting media that might be found in a PIV or PTV experiment, it was observed that the curvature of the grid lines did not vary much. Thus, it was judged that a cubic polynomial could track the distortion produced in the most common cases reasonably well. The justification for selecting quadratic dependence in  $x_3$  is due solely to the mathematical limitation that results from performing the calibration on only three  $x_3$ -planes. Generalizing the procedure to four or more planes would clearly allow higher-order terms in  $x_3$ , but for present purposes, three planes are adequate.

Before beginning the calibration procedure, one must define a coordinate system in the object plane and the image plane. The most common way to define the object-plane coordinate system is by specifying one of the characteristic marks on the face of the calibration target as the origin. The locations of all other characteristic marks are measured relative to this point. Normally, the origin of the image plane is defined by pixel (0,0) on a CCD array or the lower-left corner of a photograph. One must also make sure the experimental setup is in the exact configuration it will be in when measurements are taken.

The first step in the calibration procedure is to acquire a calibration image. This is simply an image of the calibration target as viewed by the camera in the current experimental setup. Before acquiring the image, the face of the calibration target should be aligned as precisely as possible with the center of the light sheet. Once aligned, the calibration image is acquired and stored.

The next step is to determine the locations of the characteristic marks on the calibration image with respect to the origin of the image plane. An accurate way to locate the marks is through a template-matching technique. This process is performed in a manner similar to the correlation procedure used in PIV. A template image is created that is similar to the shape of the characteristic marks on the calibration target. The template and calibration image are then correlated using two-frame cross-correlation, which is followed by a peak-searching routine to determine the pixel locations of the marks in the correlation plane. Sub-pixel accuracy can be attained by fitting a curve, such as a Gaussian or a quadratic polynomial, to the peak. Alternatively, for marks of an appropriate shape (e.g. circular), one can use a local centroid calculation, rather than template matching, to determine the locations of the marks. Once the locations of the target points in the image and object planes have been obtained, the coefficients of the mapping function in Eq. (18) can be determined using a least-squares procedure. Note that

for a single camera the calibration image is acquired at only a single  $x_3$  location (presumably at  $x_3 = 0$ ). In this case, all terms in Eq. (18) involving  $x_3$  are zero, and the corresponding coefficients are not determined by the calibration. This is acceptable because, as noted above, the single camera equations must ignore out-of-plane motion anyway.

Now that the system has been calibrated, one may proceed normally and acquire images using the conventional PIV technique. Once recorded, each image is then interrogated on a set of points  $\{\mathbf{X}_I\}$  in the image plane that is determined by the interrogation software. The image plane displacements are then validated and filtered using appropriate software tools. Note that many interrogation software systems provide the user with very limited control over the grid. Commonly, one can manipulate only a few parameters, such as the location of the grid in the image plane and the number of interrogation points to use, and specifying an arbitrary grid for interrogation is not usually possible. Even if it were, locations in the image plane are not necessarily meaningful. One would prefer to be able to request particle displacements at locations in the object plane for which the coordinates of physically meaningful locations are known.

Because it is known how positions in the object plane map to positions in the image plane from the mapping function generated during the calibration procedure, it is possible to calculate particle displacements at any location in the fluid within the domain of the mapping function. The collection of points in the object plane where displacements are desired is denoted by  $\{\mathbf{x}_g\}$  and their corresponding images by  $\{\mathbf{X}_g\}$ . The image displacements previously determined on  $\{\mathbf{X}_I\}$  during the interrogation stage are interpolated onto  $\{\mathbf{X}_g\}$  using an appropriate method, such as bilinear interpolation. Note that two potential problems can arise during this procedure. First, the image of a particular  $\mathbf{x}_g$  may lie outside the image recording domain of the camera, i.e. the CCD chip or the film frame. Second, when interpolating image displacements onto a particular  $\mathbf{X}_g$ , one or more of its neighboring grid points may not contain data. In both cases, the  $\mathbf{x}_g$  in question is discarded. At this point Eq. (11) is solved for the particle displacements in the fluid.

Fig. 3 is a flow chart that illustrates the processes described above to compute the particle displacements in the fluid. Process A represents the steps taken during the PIV experiment and ensuing interrogation process. Each step in Process A can be made within any of several different standard PIV processing software packages, including commercial software. Process B represents the procedure by which image displacements computed during process A are interpolated onto the mapping of the user-defined grid. Process C represents the calibration procedure. The results of processes B and C serve as input to Eq. (11), from which the particle displacements on the user-defined grid are calculated. Note that defining the grid  $\{\mathbf{x}_g\}$  in the object plane and mapping it onto the image plane circumvents the nonlinear inverse problem of solving for object points in terms of image location.

#### 4. Procedure for Stereoscopic Camera

The calibration procedure for a stereoscopic camera is very similar to that for a single camera (c.f. Fig. 4). However, because it is necessary to know how the magnification in the  $x_3$ -direction varies, one must acquire multiple calibration images at planes normal to the light sheet. Since a polynomial is being used to estimate the mapping function, the number of images acquired at different  $x_3$  locations places an upper limit on the order of the  $x_3$  terms. Keep in mind that a least-squares method is being used so that one could use more calibration images than the

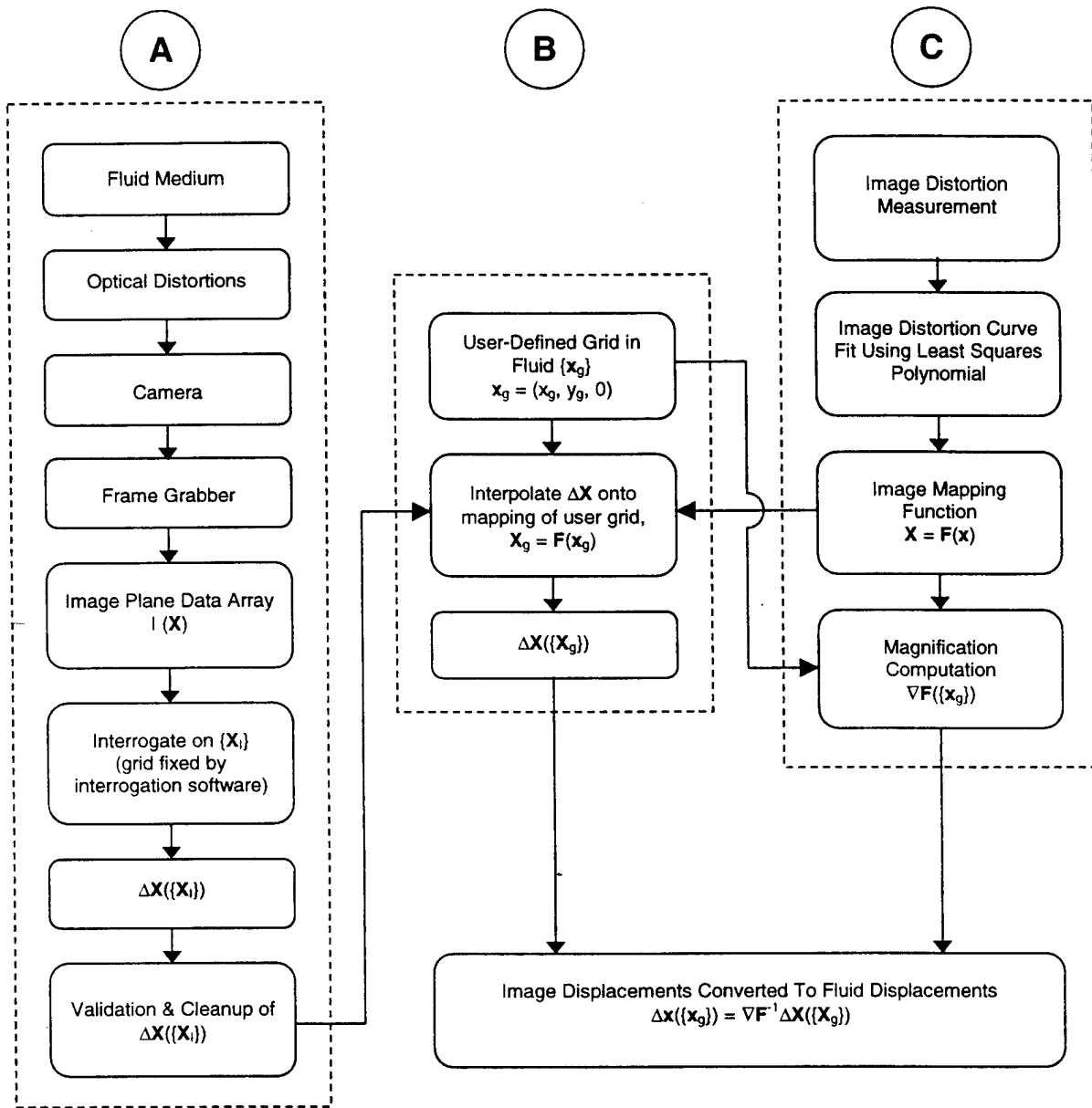


**Figure 3.** Flow chart for a single camera. Process A represents the standard PIV acquisition and interrogation procedure. Process B represents the procedure for computing displacements in the image plane corresponding to user-defined locations in the fluid. Process C represents the calibration procedure. The results of processes B and C are used to compute the particle displacements at user-defined locations in the fluid.

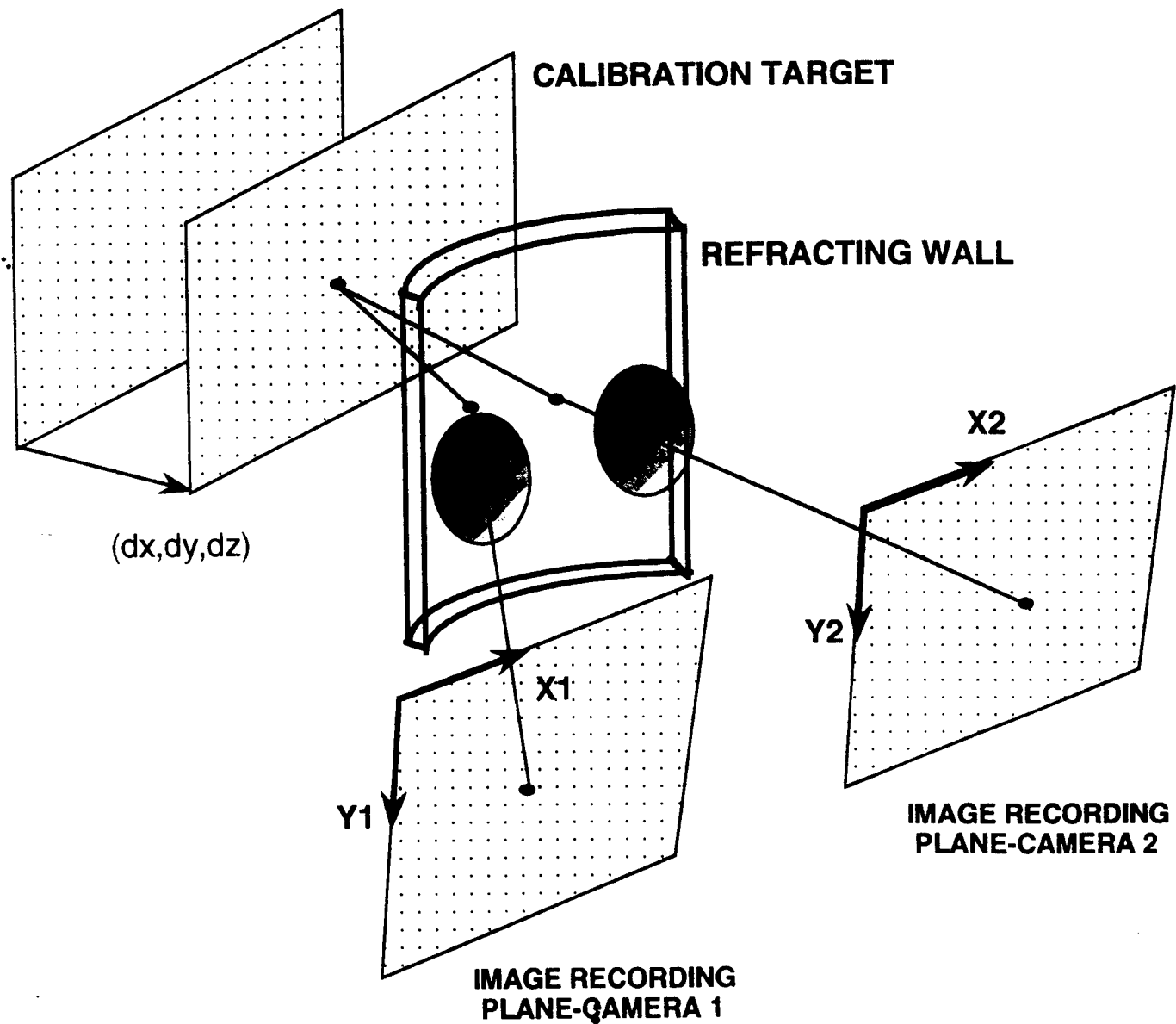


**Figure 4.** Schematic of the calibration procedure for a stereoscopic camera. The mapping function for each camera is valid over the volume of size  $dx \times dy \times dz$  traced out by the calibration target during the calibration procedure.

desired order of the  $x_3$ -terms in order to reduce the mean square error of the estimate. At a minimum, the second order polynomial in  $x_3$  requires calibration data at three  $x_3$ -locations separated by a distance comparable to the thickness of the light sheet.

Once the calibration images for all planes have been acquired for each camera, the locations of the characteristic marks in each image are determined with respect to the origin of the corresponding image plane. The same procedure described in the previous section for locating the images of the calibration marks is applied to each image. Enough information is now available to determine the coefficients in Eq. (18) twice — once for each camera. As shown in §2.2, the resulting two mapping functions are all that is necessary to recombine a pair of 2-D velocity fields into a single planar 3-D velocity field.

Once the system has been calibrated, one can proceed normally and acquire images using the conventional PIV technique. The images for each camera are interrogated on a set of points  $\{\mathbf{X}_i^{(c)}\}$  in the corresponding image plane that is determined by the interrogation software. The limitations mentioned in the previous section concerning user-control of the grid apply here, as well. The ability to specify a user-defined grid in the fluid, as in the single camera case, is applicable to the stereoscopic camera, also. The two problems that may arise during the interpolation of image displacements onto  $\{\mathbf{X}_g^{(c)}\}$  can now occur for each camera individually. If a particular  $\mathbf{x}_g$  has been deleted because of a problem that occurred during interpolation on either camera, stereo recombination cannot be performed at this location and a hole will appear in the final 3-D velocity field.

Fig. 5 is a flow chart that illustrates the processes described above to compute 3-D particle displacements in the fluid. The processes outlined in Fig. 3 are performed for each camera. The results of processes B1, B2, C1, and C2 are used to form the augmented system in Eq. (15), and the 3-D particle displacements on the user-defined grid are calculated. It should be noted that unlike the stereoscopic PIV recombination algorithm given in Prasad and Adrian (1993) in which the image plane interrogation grid and corresponding image displacements were inversely mapped into the fluid followed by the determination of a common Cartesian grid to interpolate displacements onto, the algorithm presented here requires no such procedure. The entire process is simplified by mapping the user-defined grid  $\{\mathbf{x}_g\}$  onto each image plane and performing the interpolation of displacements therein.

## 5. Application and Evaluation of Calibration Procedure

In this section, we present the results of applying the calibration procedure to both a single camera and a stereoscopic camera. In each case, a computer-generated image was displaced by a known amount in the object plane and the corresponding image displacements were computed using TSI INSIGHT PIV software. Mapping functions were used to compute the fluid displacement from this information and errors are plotted. Unless otherwise mentioned, the uncertainty in any experimental displacements of the image is  $\pm 5 \mu\text{m}$ .

### 5.1 Single Camera

The setup for the single camera experiment is shown schematically in Fig. 6. In order to test the robustness of the calibration procedure, a distorting medium was purposely placed

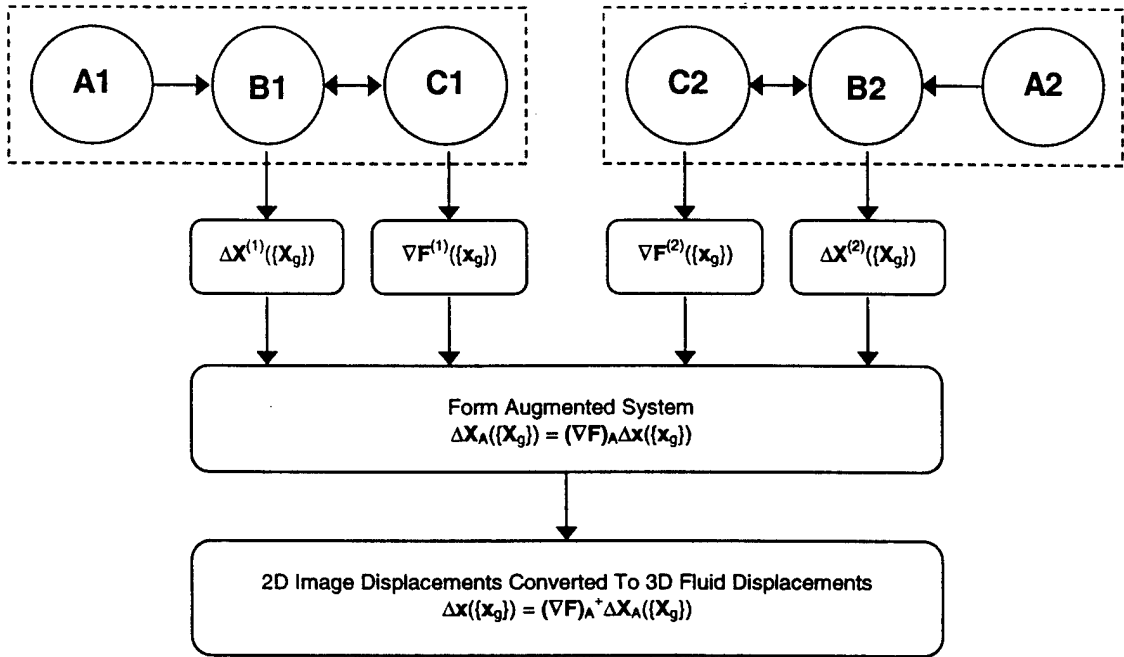


**Figure 5.** Flow chart for stereoscopic configuration. Processes A, B, and C from Fig. 3 are performed for both cameras. An augmented system is formed and solved for the 3D particle displacements at user-defined locations in the fluid. Note that  $(\nabla F)_A^+$  is the generalized inverse of  $(\nabla F)_A$ .

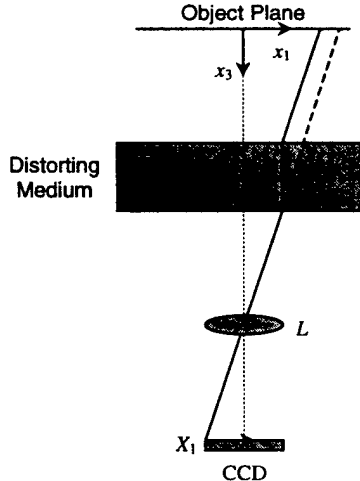


**Figure 6.** Schematic of the single camera.

between the lens and the object plane. Two lenses of focal length 450 mm placed in series were used to provide the distortion. Fig. 7(a) illustrates the effect of the distortion on a uniform Cartesian grid placed in the object plane.

The calibration target used in this experiment was a uniform  $12 \times 12$  Cartesian grid of white circles on a black background. The diameter of each circle was 1 mm, while the spacing of the circles was 5 mm in  $x$  and  $y$ . The calibration procedure was performed and the mapping

function was generated. The RMS error in the mapping function was calculated to be 0.53 pixels (corresponding to an average RMS error of  $6.9 \times 10^{-2}$  mm in the object plane). It should be noted that the RMS error is influenced by not only the ability of the least-squares polynomial to fit the data, but also by the accuracy with which image locations of the characteristic marks are measured during calibration. Prasad *et al.* (1992) have shown that the random error associated with locating particle image centroids in PIV is approximately 7% of the particle image diameter. The random error associated with the least-squares fit is approximately 6% of the particle image diameter. Thus, the accuracy of the curve fit is comparable to the accuracy for locating particle image centroids, from which it is inferred that the third-order polynomial was adequate to represent the distortion in this experiment.

To test the algorithm for computing accurate fluid displacements, a computer-generated pattern of randomly located dots was placed on a translation stage, and an image was acquired at both a reference position and after a displacement of  $\Delta x = (0.500, 1.000, 0.000)$  mm. The two images were then interrogated using two-frame cross-correlation to determine the displacements of the particle images, and the resulting vector field was validated and filtered.

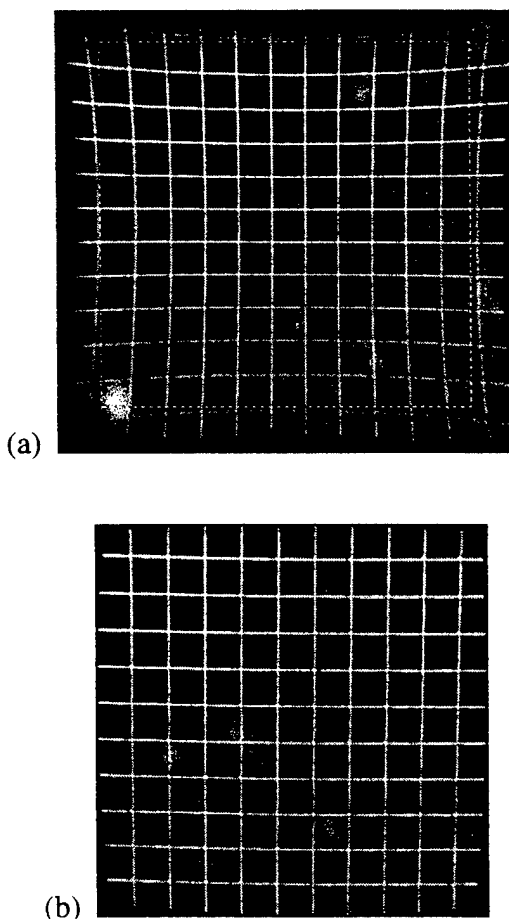


**Figure 7.** (a) Distorted image of a uniform Cartesian grid, and (b) undistorted image obtained using the mapping function from the calibration. The region of (a) that has been undistorted is indicated by the dashed rectangle.

Figs. 8 and 9 are contour plots of the error in the computed fluid displacement obtained using the displacement equations for a single camera. The error has been nondimensionalized by the size of the mapping function domain in the appropriate direction. In this experiment, the size of the domain was 55.8 mm in both  $x$  and  $y$ . This nondimensionalization was chosen in order to show how much the calculated fluid displacements are in error relative to the size of the region being mapped. The largest error in both figures is approximately 1/1000 the size of the mapping function domain. It does not appear that any trends are present in the error, implying that random error is the dominating source. However, there are several areas in both figures where the error appears to be correlated.

As noted in §2, it is possible to compute an inverse mapping function for the single camera since each  $\mathbf{X}_i$  is associated with a unique  $\mathbf{x}_i$ . Using the same calibration image previously acquired, the inverse mapping function for this setup was generated, and its RMS error was calculated to be  $1.5 \times 10^{-2}$  mm. The inverse mapping function was used to “dewarp” the grid shown in Fig. 7(a), and the dewarped grid appears in Fig. 7(b).

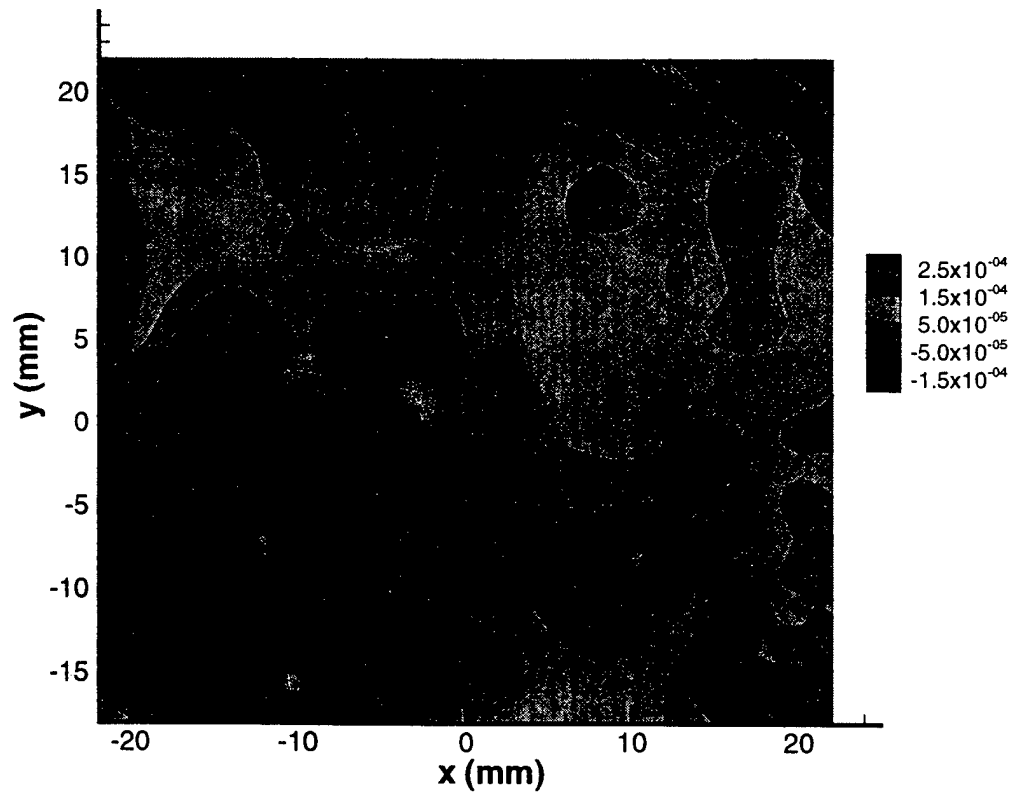


**Figure 8.** Error between the true  $x$ -displacement in the object plane and the computed value. The error has been nondimensionalized by 55.8 mm, which is the size of the mapping function domain in the  $x$ -direction.

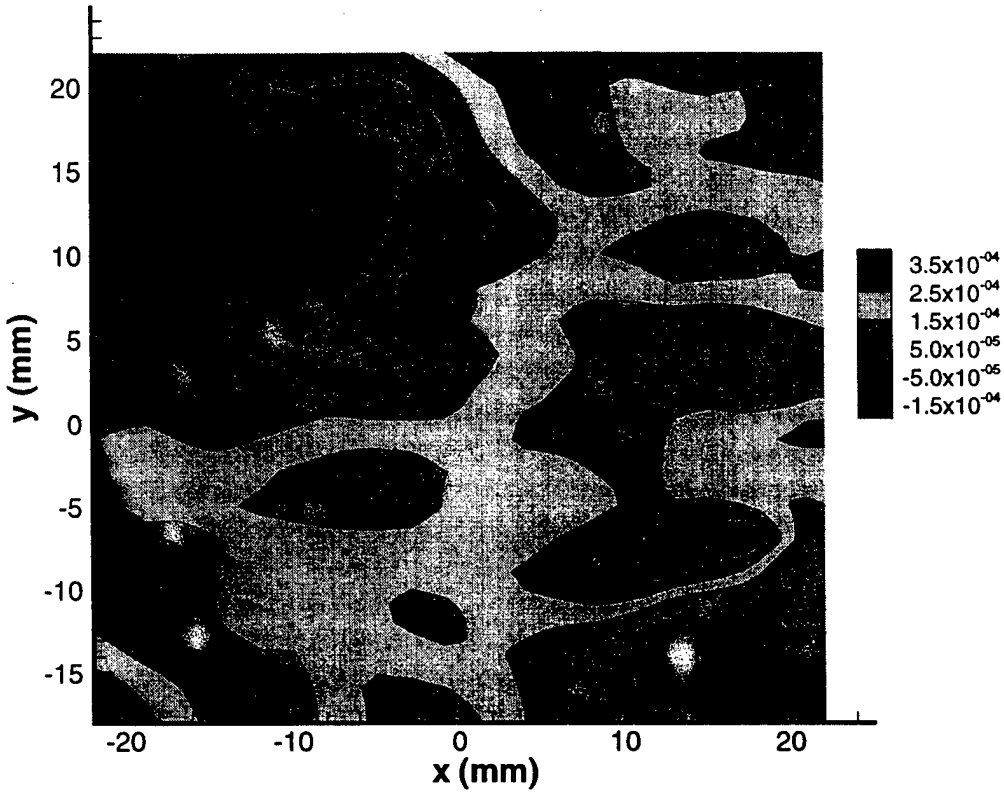


**Figure 9.** Error between the true y-displacement in the object plane and the computed value. The error has been nondimensionalized by 55.8 mm, which is the size of the mapping function domain in the y-direction.

## 5.2 Stereoscopic Camera

The stereoscopic camera is shown schematically in Fig. 10. For a detailed description of the camera configuration, see Liu *et al.* (1997). In order to test the robustness of the mapping function approach for stereo recombination, a distorting medium was purposely placed between the lenses and the object plane. A water-filled fish tank, approximately 305 mm deep, was used to provide the distortion.

The calibration target used in this experiment was a rectangular block of aluminum with 81 circular holes drilled into its face. These holes were arranged on a uniform  $9 \times 9$  Cartesian grid. The diameter of each hole was 0.5 mm, while the spacing of the holes was 9 mm in  $x$  and  $y$ . A light source placed behind the target was used to illuminate the holes. The calibration procedure was performed and the mapping function for each camera was generated. During the calibration, the target was placed at  $x_3$  locations of 0.000, 0.500, and -0.500 mm. The RMS errors in the mapping functions for cameras 1 and 2 were 1.1 pixels and 1.2 pixels, respectively. These correspond to an average RMS error of  $4.5 \times 10^{-2}$  mm and  $5.1 \times 10^{-2}$  mm in the object plane, respectively.

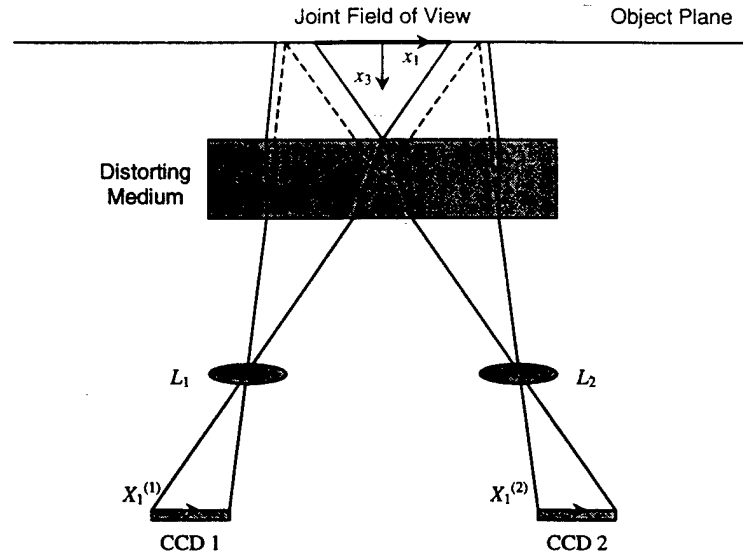


Figure 10. Schematic of the stereoscopic camera.

To test the recombination algorithm, a computer-generated pattern of randomly located dots was placed on a translation stage, and an image was acquired at a reference position and after a displacement of  $\Delta x = (0.000, 1.000, -0.400)$  mm. The two images for each camera were then interrogated using two-frame cross-correlation to determine the displacements of the particle images. The resulting 2-D vector fields were then subjected to vector validation and filtering. Finally, the stereoscopic recombination algorithm was applied and the planar 3-D velocity field was generated.

Figs. 11–13 are contour plots of the error in the computed fluid displacement obtained using the displacement equations for a stereoscopic camera. The error has been nondimensionalized by the size of the mapping function domain in the appropriate direction. In this experiment, the size of the domain was 72 mm in both  $x$  and  $y$  and 1 mm in  $z$ . As for the single camera, it appears that no trends are present in the error, but there are still correlated regions.

## 6. Summary

A procedure for calibrating both conventional and stereoscopic PIV systems has been presented. The results of the calibration yield one or more mapping functions that provide a convenient and accurate way to correct for distortion in the experiment when determining particle displacements. In particular, it is possible to accurately determine the magnification matrix that relates image plane displacements to object space displacements. In addition, a stereoscopic camera is automatically registered during the calibration procedure, which frees the user from the task of mechanically registering the camera. This permits rapid and easy setup of angular-offset stereoscopic cameras. The analysis provides accurate equations by which one solves for the 2-D or 3-D displacement of the fluid and it permits the use of arbitrary user-defined grids in the fluid.

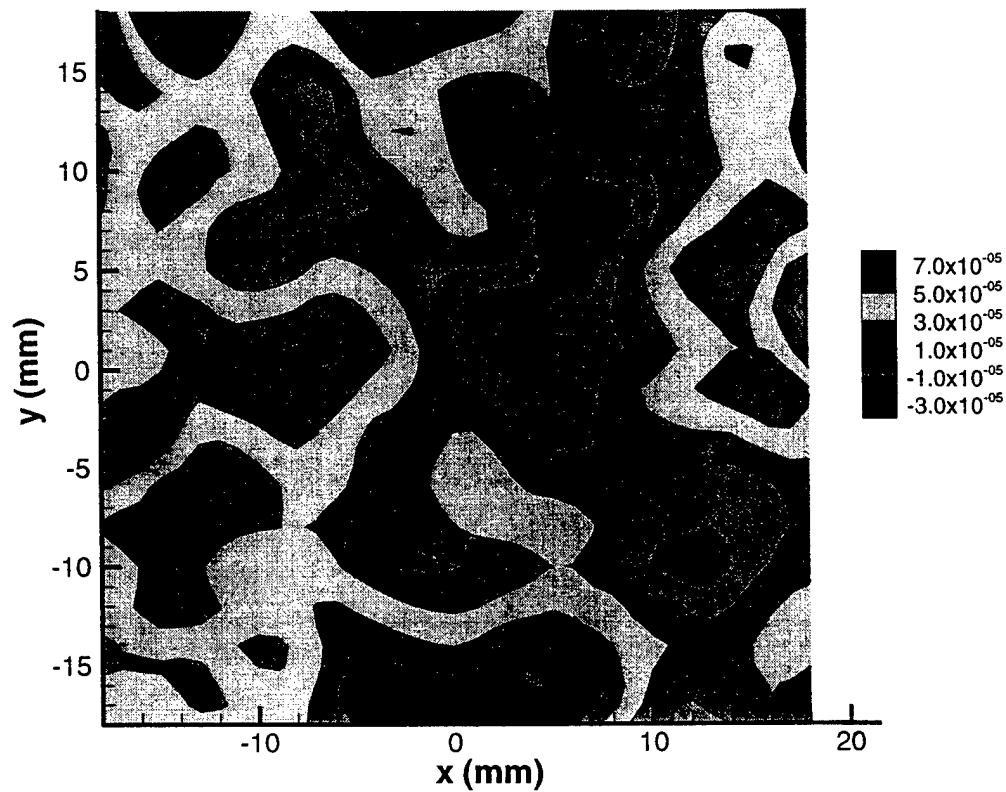


**Figure 11.** Error between the true  $x$ -displacement in the object plane and the computed value. The error has been nondimensionalized by 72 mm, which is the size of the mapping function domain in the  $x$ -direction.

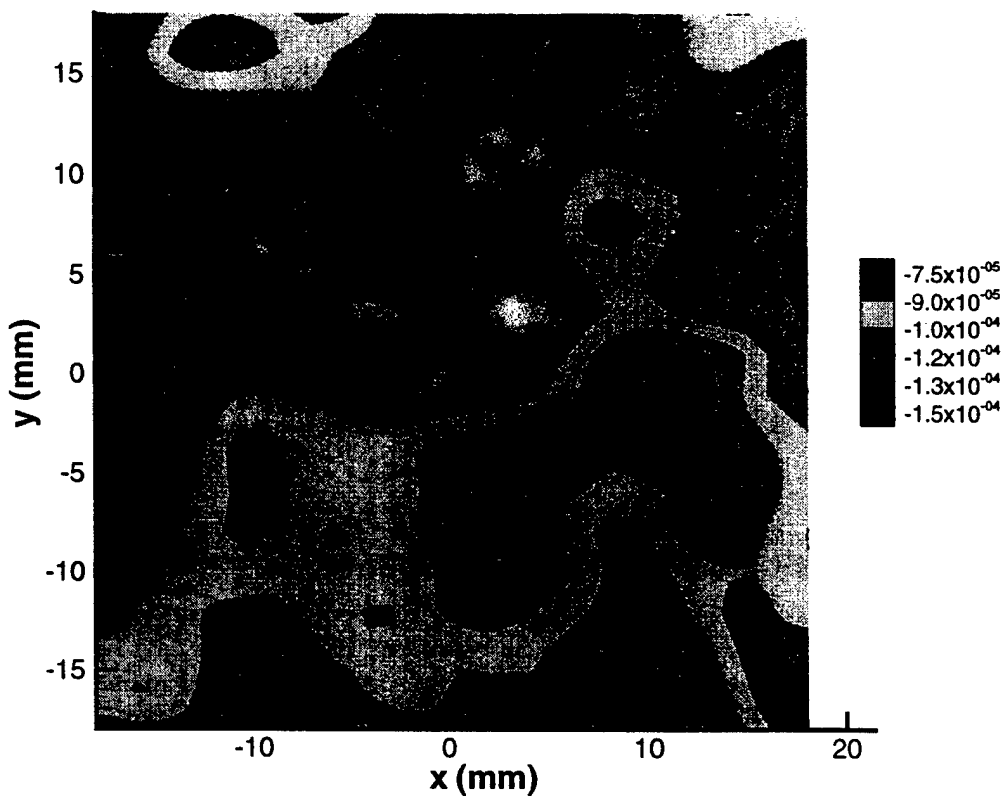


**Figure 12.** Error between the true y-displacement in the object plane and the computed value. The error has been nondimensionalized by 72 mm, which is the size of the mapping function domain in the y-direction.

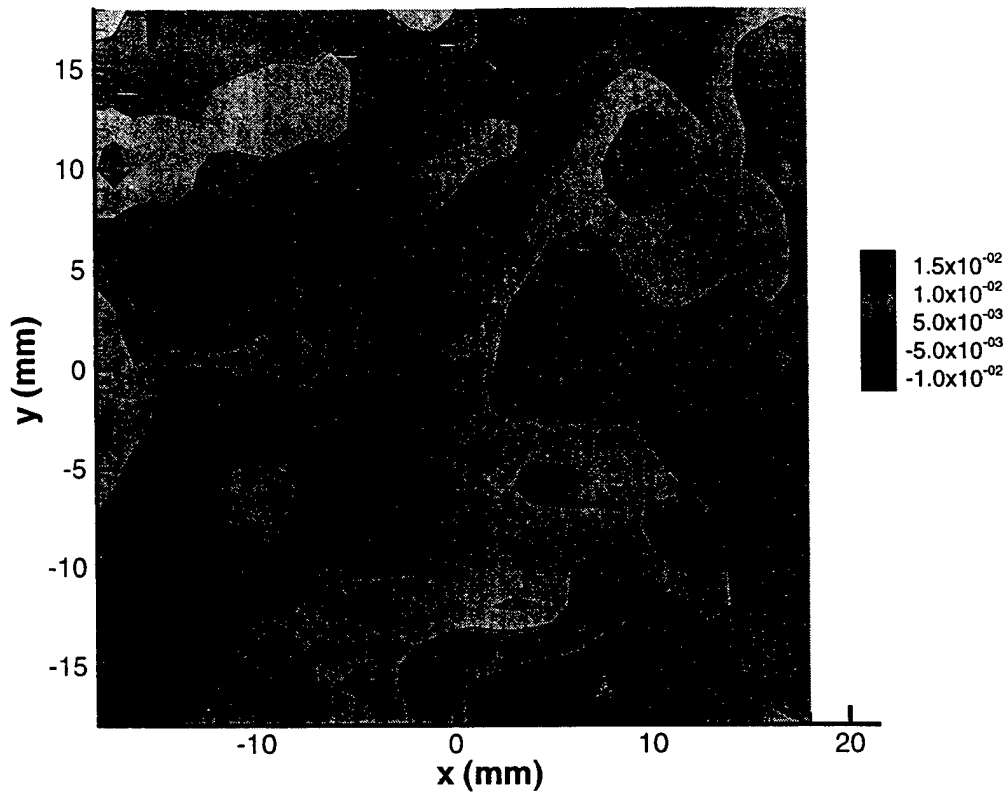


**Figure 13.** Error between the true  $z$ -displacement in the object plane and the computed value. The error has been nondimensionalized by 1 mm, which is the size of the mapping function domain in the  $z$ -direction.

## Acknowledgments

This work was supported by TSI, Inc. (St. Paul, Minnesota) and a grant from the Office of Naval Research.

## References

Adrian R J 1988 Statistical properties of particle image velocimetry measurements in turbulent flow *Laser Anemometry in Fluid Mechanics – III* ed R Adrian *et al* (Lisbon: Ladoan-Instituto Superior Técnico) pp 115–29

Adrian R J 1991 Particle-imaging techniques for experimental fluid mechanics *Ann. Rev. Fluid Mech.* **23** 261–304

Arroyo M P and Greated C A 1991 Stereoscopic particle image velocimetry *Meas. Sci. Tech.* **2** 1181–6

Grant I, Fu S, Pan X and Wang X 1995 The application of an in-line, stereoscopic, PIV system to three-component velocity measurements *Exp. Fluids* **19** 214–21

Guezennec Y G, Brodkey R S, Trigui N and Kent J C 1994 Algorithms for fully automated three-dimensional particle tracking velocimetry *Exp. Fluids* **17** 209–19

Jenkins F A and White H E 1957 *Fundamentals of Optics* (New York: McGraw-Hill) pp 130–56

Kent J C, Trigui N, Choi W-C, Guezennec Y G and Brodkey R S 1993 Photogrammetric calibration for improved three-dimensional particle tracking velocimetry *Optical Diagnostics in Fluid and Thermal Flow* ed S Cha and J Trolinger (Bellingham, WA: SPIE) pp 400–12

Liu Z-C, Adrian R J, Meinhart C D and Lai W 1997 Structure of a turbulent boundary layer using a stereoscopic, large format video-PIV to appear in *Developments in Laser Techniques and Fluid Mechanics* ed R Adrian *et al* (Berlin: Springer)

Maas H G, Gruen A and Papantoniou D 1993 Particle tracking velocimetry in three-dimensional flows. Part 1. Photogrammetric determination of particle coordinates *Exp. Fluids* **15** 133–46

Nishino K, Kasagi S and Hirata M 1989 Three-dimensional particle tracking velocimetry based on automated digital image processing *ASME J.* **111** 384–91

Prasad A K, Adrian R J, Landreth C C and Offutt P W 1992 Effect of resolution on the speed and accuracy of particle image velocimetry interrogation *Exp. Fluids* **13** 105–16

Prasad A K and Adrian R J 1993 Stereoscopic particle image velocimetry applied to liquid flows *Exp. Fluids* **15** 49–60

Prasad A K and Jensen K 1995 Scheimpflug stereocamera for particle image velocimetry in liquid flows *Appl. Opt.* **34** 7092–9

Table 1.

Item	PIV System	Proposed Vendor Name (Actual Vendor Name)	Proposed	Actual	Account #	PO #	Inv. #
Nd: YAG Laser	DPIV	Continuum (Stanford Research Sys)	30,000	20000.00	1-5-20513	JX56925FE	C42879
Misc. Laser Optics	DPIV	Melles-Griot (Helix) (Melles-Griot) (Melles-Griot) (Melles-Griot) (Melles-Griot) (Melles-Griot) (Calumet/Chicago) (Pinnacle Micro, Inc.)	5,000	4238.25 1522.00 2365.59 1514.88 2770.86 54.46 60.39 357.66 1146.56 51.44	1-5-20513 1-5-20513 1-5-20513 1-5-20513 1-5-20513 1-2-23660 1-5-20513 1-2-23660 1-2-23660 1-2-23660	JXS0531E JXQ5345E C59147 C59149-50 C59147 C59206/7 C59206/7 C59206 C59206/7	C42892 C59147 C59149-50 C59147 C59206/7 C59206/7 C59206 C59206/7
Kodak Megaplus CCD Cam	DPIV	Panatek, Inc. (Eastman) (TSI, Inc.)	50,000	49528.76 33329.20	1-5-20513 1-5-90763	JX54884FE JX45914FE	C56104-5 C56069
Univision Frame Grabber	DPIV	Panatek, Inc. (Eastman) (TSI, Inc.) (BitFlow, Inc.)	16,160	16286.83 16286.83 980.50	1-2-68957 1-2-23660 1-5-20513	JX55407FE JX55407FE JXS0612D	C56096 C56097 cables
IBM Misc 6000 Computer	DPIV	Rand Tech. (TSI, Inc. see above) (Aclaron or Microway) (IBM via Central Stores)	29,831				
PIV Analysis Software	DPIV	TSI, Inc.	25,000	25000.00	1-6-41778	yes	software
Nd:YAG Laser	HPIV	Lightwave (Coherent)	28,500	28016.64	1-5-20513	JX56354FE	C56087
Imaging Tech. Frame Grab	HPIV	Panatek, Inc. (Eastman) (Data Translation)	9,230				
SGI Indigo Computer	DPIV/HPIV	Silicon Graphics (and Habers)	28,500	28883.40 2225.00 2225.00	1-5-20513 1-2-23660 1-2-68957	JX54745LE JX56400LE JX56400LE	C56071-74 C56081 C56081
X Terminal	DPIV/HPIV	(Iomega via Central Stores)		285.00	1-2-68957	GS113137/307	
4GB Hard Disk	DPIV/HPIV	Sun Express (Data Comm Warehouse) (NCA Peripherals) (DC Drives) (PC MacConnection) (Computability)	2,790	1147.50 419.90 408.00 1740.00 354.95 1298.00	1-5-20513 1-5-20513 1-5-20513 1-5-20513 1-5-20513	JXS0625E JXQ5229E JXQ5230E JXQ5341E JXQ5338E JXQ5342E	C56101 inc. C56096 inc. C56096 C56097 inc. G01756 C59146
8GB DAT Stores Tape Dr	DPIV/HPIV	MacWarehouse	1,600				
Macintosh Computer	DPIV/HPIV	Central Stores	5,000	62.00 56.81	1-2-23660 1-2-68957	SR742349 JXQ5344D	software cables
Laser Printer	DPIV/HPIV	Sun Express	4,598				
Color Laser Printer	DPIV/HPIV	Sun Express (Aerotech) (Freight)	3,295				
				677.00 10.65	1-2-23660 1-2-23660	JXW2341A FT116297	drive module to Pinnacle
				253,589	253589.00		
					153589.00	1-5-20513	
					20000.00	1-2-68957	
					21670.80	1-2-23660	
					33329.20	1-5-90763	
07/23/97					25000.00	1-6-41778	TSI donation

Donor Name:	TSI, Inc.
Care of or attention of:	Dr. Wing Li
Street:	500 Cardigan Road
Street:	P.O. Box 64204
City, State, Zip:	St. Paul, MN 55164

ATTACH COPIES OF ANY CORRESPONDENCE AND ENVELOPES

Software donation for use in particle image analysis system  
purchased from TSI, JX55407FE

ATTACH -- PAS FORM 11, NON-CASH ADDITIONS -- FOR GIFT IN KIND

Quotation #R2-189-2 dated 01/31/95

See attached.

25000.00	06/15/95	Check Number Valuation Method	quotation	Date Chq.	n/a
----------	----------	----------------------------------	-----------	--------------	-----

## RECIPIE

Acct Number	1 -0- 37529	-4100	Account Title	TSI, Inc.
----------------	-------------	-------	------------------	-----------

GR 022115

Campus/College  
Department  
Code

1 22 60	Department Name	Theoretical & Applied Mechanics, 216 Talbot Lab, MC-262
---------	--------------------	---

Person to Contact  
for Additional  
Information

Sydney Cromwell	Phone	3-2323
-----------------	-------	--------

Sydney Cromwell	Date Prepared	06/07/96
-----------------	------------------	----------

## REVIEW

Reviewed By	Date Reviewed
-------------	------------------

## ACCEPTANCE

Signature	Date Accepted
-----------	------------------

## Quotation

## TSI Incorporated

Fluid Mechanics Instrument Division

500 Cardigan Road 612 490 2811  
P.O. Box 64204 Telex 6879024  
St. Paul, MN 55164 USA Fax 612 490 3824

TO Dr. Ronald J. Adrian  
 University of Illinois  
 Theoretical & Applied Mech.  
 216 Talbot Laboratory  
 104 S. Wright St.  
 Urbana, IL 61801-2935  
 (217) 333-1793 - Phone  
 (217) 244-5707 - Fax

Quote No. R2-189-2 (Page 1 of 2)  
 Quote Date January 31, 1995  
 Customer Ref.  
 Due Date  
 Terms: Net 30 Days  
 Firm Quote for 90 Days  
 Prices are F.O.B. St. Paul, MN U.S.A.

Item No.	Quantity	TSI Model No.	Description	Unit Price	Extended Total
1.	1	600031	Insight PC Window based PIV Analysis Software Acquisition and Processing Module with * Support for both film based and video based PIV data * Selectable pixel resolution and user configurable grid size * 2-D auto and cross correlation * Real-time control and manipulation on image file * Open Image format * 1-5 vectors/sec at 486 based computer * 10-40 vectors/sec with array processor Post Processing Module with * Automated Data Validation and Recovery * Multiple Window Display * Velocity Averages and Derivatives * Printer Support	\$ 8,000	\$ 8,000.00
2.	1	600041	Insight Unix Workstation based PIV Analysis Software Acquisition and Processing Module with * Support for both film based and video based PIV data * Selectable pixel resolution and user configurable grid size * 2-D auto and cross correlation * Real-time control and manipulation on image file * Open Image format * 10-100 vectors/sec output Post Processing Module with * Automated Data Validation and Recovery * Multiple Window Display * Velocity Averages and Derivatives * Printer Support	10,000	10,000.00

Delivery Terms 6 weeks ARO

This Quotation is subject to the warranties, disclaimers and all other terms and conditions set forth on the reverse side hereof and to no others. Seller reserves the right to change prices effective on any new orders, provided Seller notifies in writing those with currently valid Quotations prior to any order being placed. This

quotation shall become an agreement binding upon the Buyer and the Seller when accepted by the Buyer and subsequently accepted by an authorized representative of the Seller at the Seller's home office and thereupon shall constitute the entire agreement between the parties.

Accepted By Buyer

By: \_\_\_\_\_

TSI Incorporated (The Seller)

Martin Abbott

Sales Manager - Midwest Region

## Quotation

TSI.

TSI Incorporated

Fluid Mechanics Instrument Division

500 Cardigan Road 612 490 2811  
P.O. Box 64204 Telex 6879024  
St. Paul, MN 55164 USA Fax 612 490 3824

TO Dr. Ronald J. Adrian  
University of Illinois  
Theoretical & Applied Mech.  
216 Talbot Laboratory  
104 S. Wright St.  
Urbana, IL 61801-2935  
(217) 333-1793 - Phone  
(217) 244-5707 - Fax

Quote No. R2-189-2 (Page 2 of 2)  
Quote Date January 31, 1995  
Customer Ref.  
Due Date  
Terms: Net 30 Days  
Firm Quote for 90 Days  
Prices are F.O.B. St. Paul, MN U.S.A.

Item No.	Quantity	TSI Model No.	Description	Unit Price	Extended Total
3.	1	600031X	<p>Software support for 2 frame grabbers</p> <p>Total F.O.B. Factory, St. Paul, MN:</p> <p>-----</p> <p><b>"The above quoted prices do not include applicable sales tax. If non-taxable, please provide a tax exemption certificate with your purchase order."</b></p>	\$7,000	\$7,000.00 <u>\$25,000.00</u>

**Delivery Terms** 6 weeks ARO

This Quotation is subject to the warranties, disclaimers and all other terms and conditions set forth on the reverse side hereof and to no others. Seller reserves the right to change prices effective on any new orders, provided Seller notifies in writing those with currently valid Quotations prior to any order being placed. This

quotation shall become an agreement binding upon the Buyer and the Seller when accepted by the Buyer and subsequently accepted by an authorized representative of the Seller at the Seller's home office and thereupon shall constitute the entire agreement between the parties.

**Accepted By Buyer**

By:

**TSI Incorporated (The Seller)**

Martin Abbott

### **Sales Manager - Midwest Region**